Pressure dependence and mechanism of Mn promotion of silica-supported Co catalyst in the Fischer-Tropsch reaction

Journal of Catalysis 425 (2023) 181–195

Contents lists available at ScienceDirect

Journal of Catalysis

journal homepage: www.elsevier.com/locate/jcat

Pressure dependence and mechanism of Mn promotion of silica-supported Co catalyst in the Fischer-Tropsch reaction

Tobias F. Kimpel, Jin-Xun Liu [1], Wei Chen, Robert Pestman *, Emiel J.M. Hensen *

Eindhoven University of Technology, Laboratory of Inorganic Materials Chemistry, Schuit Institute of Catalysis, Department of Chemical Engineering and Chemistry, P.O. Box 513, 5600 MB Eindhoven, the Netherlands

ARTICLE INFO

Article history:
Received 7 April 2023
Revised 2 June 2023
Accepted 6 June 2023
Available online 9 June 2023

Keywords:
Fischer-Tropsch
Cobalt
Manganese
Promotion
Pressure

ABSTRACT

The mechanism of Mn promotion of a silica-supported Co catalyst in the Fischer-Tropsch reaction has been studied at varying pressures up to 20 bar. IR spectroscopy in combination with DFT calculations suggest adsorbed CO is activated by reaction with an oxygen vacancy in the MnO, which covers the Co surface. This leads to a higher activity, higher CH_x coverage and thus higher C_{5+} and lower CH_4 selectivity. Increasing the pressure magnifies the selectivity differences. However, above around 4 bar, the effect of Mn on the selectivities is reversed and the C_{5+} selectivity is decreased by Mn addition. This is tentatively attributed to Mn promoting the C-O bond dissociation but not the chain growth. Formed monomers have to migrate to stepped sites for chain growth on the Co surface. Whilst this is migration is not impeded by co-adsorbates at low pressure, migration could be hindered by especially the high CO coverage at high pressure.

1. Introduction

The Fischer-Tropsch (FT) reaction is a catalyzed reaction, in which hydrocarbons and water are formed from synthesis gas (a mixture of CO and H_2). Several large-scale industrial plants have been constructed based on synthesis gas derived from either coal or natural gas. The interest for FT synthesis in future energy scenarios stems from the possibility to obtain synthesis gas from renewable sources such as biomass or from CO_2 using renewable hydrogen. Whereas most group VIII transition metals exhibit activity in the Fischer-Tropsch synthesis, only Fe and Co have been used as industrial FT catalysts. For FT synthesis using coal-derived synthesis gas with a low H_2/CO ratio, Fe-based catalysts are preferred due to their high water–gas shift activity. When synthesis gas is derived from natural gas, supported Co catalysts are typically used because of their higher activity and higher chain-growth probability in combination with a low water–gas shift activity [1,2,3].

A serious drawback of Co– and Fe-catalyzed FT is the high methane yield, which often even exceeds the yield predicted by the Anderson-Schulz-Flory (ASF) distribution for polymeric chain growth [4]. Therefore, a lot of research has concentrated on decreasing the methane selectivity and increasing the selectivity to desired longer-chain hydrocarbons. For this purpose, addition of promoters has been studied extensively. Metal promoters (e.g., Cu, Pt, and Re) are known to increase the reducibility or dispersion of the active phase, but they hardly improve the selectivity [5]. On the other hand, oxides of metals such as Mn, V, Th, Ce, and Cr can improve the selectivity. Their promotional mechanism is however uncertain [5,6].

Since 2000, a large number of studies has been devoted to Mn-promoted Co catalysts [7–13]. It was found that the use of Mn can enhance the activity and suppress hydrogenation, leading to a higher chain-growth probability (α) and lower methane selectivity. However, many of the catalytic performance tests in these studies were performed at ambient pressure, which is quite different from the industrially used pressure (10 to 30 bar). Moreover, studies employing elevated pressure report contradicting results regarding the influence of Mn on the olefins-to-paraffins (O/P) ratio and the product distribution (C_{5+} and methane selectivity). In the past, the manganese promotion effect was ascribed to faster CO dissociation due to the binding of the oxygen atom of adsorbed CO to the Mn redox center [14–16]. The group of Bel [6,17,18]l developed a mechanistic model for Mn promotion where Mn^{2+} acts as a Lewis acid, which would facilitate the dissociation of CO. This hypothesis was supported by studying a wide range of metal oxides that showed a similar enhancement of the catalytic performance [6]. Mn has also been said to enhance Co_2C formation [19,20]. Thus,

* Corresponding authors.
E-mail addresses: r.pestman@tue.nl (R. Pestman), e.j.m.hensen@tue.nl (E.J.M. Hensen).
[1] University of Science and Technology of China, Department of Chemical Physics, School of Chemistry and Materials Science, Hefei, China.

https://doi.org/10.1016/j.jcat.2023.06.010
0021-9517/

the nature of Mn promotion has not been resolved yet. Theoretical studies have shown that Co catalysts operate in the monomer formation limit, in which the dissociation of the C-O bond is the rate-limiting step [21]. As a result, it seems reasonable to assume that Mn helps to dissociate CO. However, experimental proof is still missing. The aim of this paper is to shed light on the mechanism of Mn promotion on silica-supported Co catalyzed FT at industrial reaction pressures. Catalytic tests were performed at low and medium pressure. Based on the activity data in combination with *in situ* IR experiments, steady-state isotopic kinetic analysis (SSITKA), and density functional theory (DFT) calculations, the mechanism of Mn promotion in the Co catalyzed FT is discussed.

2. Experimental methods

2.1. Catalyst preparation

The silica-supported Co catalysts were prepared by incipient wetness impregnation of SiO_2 (Shell, sieve fraction 120–250 μm, 136 m^2/g) with an aqueous solution of $Co(NO_3)_2{\cdot}6H_2O$ (Merck, 99.99%) and $Pt(NH_3)_4{\cdot}(NO_3)_2$ (Alfa Aesar, 99.995%). Pt (0.04 wt%) was added as a reduction promoter. To study the effect of Mn promotion, $Mn(NO_3)_2{\cdot}xH_2O$ was added to the solution at atomic Mn/Co ratios of 0.05, 0.1 and 0.25. The impregnated catalysts were dried at 80 °C in a flow of 80 vol% He and 20 vol% O_2 for 2 h, followed by calcination at 350 °C for 2 h (heating rate 2 °C/min). The Co and Mn loadings were determined by ICP-OES elemental analysis (Spectroblue, AMETEK Inc.) after dissolution in concentrated HCl. The silica supported Co-only catalyst is denoted as Co/Si. The Mn-promoted Co catalysts are referred to as CoMn(x)/Si with $\times$ being the atomic Mn/Co ratio.

2.2. Catalyst characterization

2.2.1. In situ X-ray diffraction (XRD)

In situ X-ray diffraction (XRD) patterns were obtained on a Rigaku D/max-2600 X-ray diffractometer. The size of the Co-oxide particles in the calcined catalysts was estimated by applying the Scherrer equation to the (3 1 1) reflection of the as-prepared Co_3O_4 phase. Based on the particle size of the cobalt oxide, an estimation could be made of the metal particle size obtained after reduction by multiplication with a factor of 0.75.[22] The structural evolution during reduction of the oxidic catalyst precursor was monitored by *in situ* XRD: The samples were reduced at 450 °C with a rate of 5 °C/min in a flow of 10 vol% H_2 in He. XRD patterns were recorded every 25 °C.

2.2.2. Hydrogen-Temperature programmed reduction (H_2-TPR)

H_2-TPR measurements were conducted in a Micromeritics AutoChem II 2920 apparatus. In a typical experiment, 50 mg of sample was dried in a flow of He for 1 h at 100 °C before ramping to 1000 °C at a rate of 10 °C/min in a flow of 4 vol% H_2 in He.

2.2.3. In situ XPS

The oxidation state of Co and Mn was characterized using quasi *in situ* XPS in a Kratos AXIS Ultra 600 spectrometer equipped with a monochromatic Al Kα X-ray source (Al Kα 1486.6 eV). Survey scans were recorded at a pass energy of 160 eV, detailed region scans at 40 eV. The step size was 0.1 eV in both cases. The background pressure during the measurements was kept below $5 \cdot 10^{-9}$ mbar. A high-temperature reaction cell (Kratos, WX-530) was used to pretreat the sample. The sample was supported on an alumina stub, allowing *in vacuo* transfer of the sample into the measurement chamber. Reduction was performed in an equimolar mixture of H_2 and Ar flow at atmospheric pressure at 450 °C for 8 h. After reduction, the sample was allowed to cool to 150 °C and subsequently evacuated and transferred to the measurement chamber. The XPS data were analyzed with CasaXPS (version 2.3.16 PR 1.6) software.

2.2.4. Transmission electron microscopy (TEM)

TEM measurements were performed with a FEI Tecnai 20 electron microscope at an electron acceleration voltage of 200 kV with a LaB_6 filament. A few milligrams of sample were ultra-sonicated in ethanol and dispersed over a carbon-coated Cu grid. The average particle size and particle size distribution were determined by measuring at least 100 particles.

2.2.5. H_2-chemisorption

The metal surface area of the reduced catalysts was determined by H_2-chemisorption in a Micromeritics ASAP 2010 apparatus. After reduction of typically 200 mg of catalyst in a flow of 2 vol% H_2 in He at 450 °C, the sample was evacuated for 30 min at 470 °C to desorb chemisorbed hydrogen. H_2 uptake was determined at 110 °C. The available metal surface area was calculated assuming that one H atom adsorbs per surface Co atom.

2.2.6. Infrared (IR) spectroscopy

IR spectra were recorded with a Bruker Vertex V70v instrument by averaging 32 scans at 2 cm^{-1} resolution. Typically, 15 mg sample was pressed into a self-supporting wafer with a diameter of 13 mm and placed in a homemade controlled-environment transmission IR cell. Prior to IR measurements, the sample was reduced in a flow of H_2 at 450 °C for 4 h using a heating rate of 5 °C/min. After evacuation at 450 °C for 30 min, the sample was cooled *in vacuo*. Before dosing CO, a background spectrum was recorded. CO was dosed using a sample loop of 10 μl connected to a 6-way valve.

Temperature-programmed IR (TP-IR) spectra were recorded in the presence of either CO (10 mbar) or synthesis gas (60 mbar H_2, 30 mbar CO) in the temperature range of 50 to 300 °C. For these TP-IR measurements, the number of scans was reduced to 16.

2.3. Catalytic performance measurements

The catalytic performance of the Co samples was determined in a Microactivity Reference unit (PID Eng&Tech) at a temperature of 220 °C and a pressure of 20 bar. In a typical experiment, 150 mg catalyst was homogenously mixed with SiC particles of the same sieve fraction to yield a constant bed volume of 3 ml. The mixture was placed in a tubular reactor with an internal diameter of 9 mm resulting in a catalyst bed height of 4.7 cm. The reactor temperature was controlled using a thermocouple located at the center of the catalytic bed. The samples were reduced by heating to 450 °C at a rate of 3 °C/min in an equimolar flow of H_2 and He, followed by a dwell of 8 h. Subsequently, the reactor was cooled to 220 °C and the gas feed was replaced by the reaction mixture, which was synthesis gas with a H_2/CO ratio of 2 diluted with He (volumetric He/H_2/CO = 40/40/20) and containing 4 vol% Ar as an internal standard. The gas-hourly space velocity (GHSV) of the total gas flow was 1000 h^{-1}, which resulted in typical conversion levels in the range of 5 to 15%. A TRACE 1300 gas chromatograph of Thermo Scientific Instruments equipped with a TCD and FID was used to analyze the effluent reaction mixture. Liquid products and waxes were collected in a rearward cold trap. Hydrocarbons (C_1 to C_{12}) were analyzed using an Rt-Silica BOND column equipped with an FID. The analysis of light gasses H_2, CO_2, CH_4, C_2H_4, C_2H_6, Ar, and CO was performed with Molsieve 5A (mesh 60/80, 2 m) and two Rt-XL Sulfur columns (0.25 m and 1 m) in combination with a TCD. Under the studied reaction conditions, CO_2 was not detected as a reaction product and the carbon-based selectivity of

oxygenates was lower than 1 %. The CO conversion (X_{CO}) was determined based on Eq. (1), the carbon based selectivity to product *i* with i carbon atoms (S_i) based on Eq. (2), and the reaction rate (r_{CO}) was based on Eq. (3). The turnover frequencies of the CO conversion, (TOF_{CO}) and methane formation (TOF_{CH_4}) were based on Eqs. (4) and (5), respectively.

$$X_{CO} = \left(1 - \frac{\frac{CO_{out}}{Ar_{out}}}{\frac{CO_{in}}{Ar_{in}}}\right) \quad (1)$$

$$S_i = \frac{Ar_{in} * v_i * C_i}{Ar_{out} CO_{in} X_{CO}} * 100\% \quad (2)$$

$$r_{CO} = \frac{F^0_{CO} X_{CO}}{m_{Co}} \quad (3)$$

$$TOF_{CO} = \frac{X_{CO} * F^0_{CO}}{n_{CO} * D_{H2}} \quad (4)$$

$$TOF_{CH_4} = \frac{X_{CO} * F^0_{CO} * S_{CH4}}{n_{CO} * D_{H2}} \quad (5)$$

Where CO_{in} and CO_{out}, and Ar_{in} and Ar_{out} represent the CO and Ar concentration in the inlet and outlet flow, respectively. v_i stands for the number of carbon atoms in species *i*, F^0_{CO} represents the inlet flow of CO (mol/s), m_{Co} the mass of cobalt (g), n_{CO} the number Co atoms (mol), and D_{H2} the dispersion as determined by H_2 chemisorption.

2.4. Steady-state isotopic transient kinetic analysis (SSITKA)

The coverages and residence times of reaction intermediates under steady-state conditions were determined by SSITKA. The details of the SSITKA setup have been described elsewhere [23]. Typically, an amount of 200 mg catalyst diluted with SiC of the same sieve fraction was loaded in a low dead-volume stainless-steel tubular reactor with an inner diameter of 5 mm and a bed length and of 80 mm. The sample was reduced at 450 °C using a rate of 3 °C/min at ambient pressure for 8 h in a flow of 50 ml/min consisting of 10 vol% H_2 in Ar. Subsequently, the reactor was cooled to 220 °C in an Ar flow and the pressure was increased to 1.85 bar. Afterwards, the reactor feed was switched to a mixture of ^{12}CO, H_2, and Ar. The CO flow was varied to change the H_2/CO ratio, while the Ar flow was used to adjust the total flow rate to 50 ml/min. After 16 h, a SSITKA switch was made from $^{12}CO/H_2$/Ar to $^{13}CO/H_2$/Ne. The transients of ^{12}CO (m/z = 28) and ^{13}CO (m/z = 29), the main hydrocarbon product $^{12}CH_4$ (m/z = 15) and $^{13}CH_4$ (m/z = 17), and the inert tracers (Ne (m/z = 22) and Ar (m/z = 40) were recorded by online mass spectroscopy (quadrupole mass spectrometer, ESS, GeneSys Evolution). Surface residence times were calculated via the area under the normalized transient curves N_i, whilst a correction was applied for the gas-phase hold-up with the use of the inert Ne tracer:

$$\tau_i = \int_0^\infty (N_i - N_{Ne}) dt \quad (6)$$

The residence time of the CH_x intermediate (precursor to CH_4) was corrected for the chromatographic effect of CO by subtracting half of the CO residence time by [24]:

$$\tau_{CH_4}(corrected) = \tau_{CH_4} - \frac{1}{2}\tau_{CO} \quad (7)$$

The amount of reversibly adsorbed CO and CH_x species can be estimated from the residence time and effluent flow of these species. The coverage of these two species (θ_i) was calculated by dividing the amount of adsorbed species by the number of Co surface atoms as determined by H_2-chemisorption.

$$\theta_{CO} = \frac{\tau_{CO} F_{CO} (1 - X_{CO})}{D_{H2}} \quad (8)$$

$$\theta_{CH_4} = \frac{\tau_{CH_4} F_{CO} X_{CO} S_{CH_4}}{D_{H2}} \quad (9)$$

where F_{CO} refers to the CO feed, X_{CO} and S_{CH_4} refer to the CO conversion and CH_4 selectivity as determined by online GC.

2.5. Density functional theory (DFT) calculations

All spin-polarized DFT calculations were performed using projector augmented wave (PAW) [25] potentials and the Perdew–Burke–Ernzerhof (PBE) functional [26] as implemented in the Vienna ab initio simulation package (VASP) [27,28]. The model structure for MnO consisted of an Mn_4O_4 cluster placed on the dense (0001) surface of hcp Co. The Co(0001) surface unit cell was a p(3 × 3) slab model with three atomic layers of Co. Details about the genetic algorithm (GA) used to identify the global minimum structure of the Mn_4O_4 cluster on the Co(0001) surface have been given elsewhere [29]. To accelerate the GA calculations, the cutoff energy was limited to 300 eV, the convergence threshold for geometry optimization was set to 10^{-3} eV, and Brillouin zone sampling was restricted to the Γ point. The GA optimization procedure yielded 600 structures in 80 cycles. The dissociation reaction energy diagrams of CO at the interface of Co and MnO was determined by using the most stable Mn_4O_4/Co(0001) structure. The calculated reaction pathways were inspired by pathways explored earlier for an Mn_4O_4/Ni(111) model [29]. The cutoff energy for the valence electrons was 400 eV. The geometry optimization was converged until the maximal residual force was smaller than 0.02 eV/Å and the electronic self-consistent field was converged to $1 \cdot 10^{-4}$ eV. Neighboring slabs were separated by a vacuum of 15 Å to avoid self-interactions. A Monkhorst-Pack k-points sampling of 2 × 2 × 1 was employed [30]. Transition states were located by the force reversed [31] and climbing-image nudged elastic band (CI-NEB) [32,33] methods with a force tolerance of 0.02 eV/Å.

3. Results and discussion

3.1. Catalyst characterization

The characterization results of the Co catalysts are displayed in Table 1. The Co loading is slightly lower than the intended 20 wt%, which is likely due to the presence of crystal water in the metal salt precursors. The atomic Mn/Co ratios are as targeted. Particle sizes are either based on XRD (see Fig. 1) or TEM (see Fig. S1 in the Supporting Information). The XRD pattern in Fig. 1 shows that Co_3O_4 is the only crystalline phase in the calcined precursors. The broad scattering feature around 23° is typical for amorphous silica. The XRD patterns do not contain indications of separate Mn-oxide phases. However, with increasing Mn content a shift to lower angles is observed in the diffraction pattern of Co_3O_4 together with a broadening of the reflections (see Fig. 1b). These changes indicate incorporation of Mn in the spinel structure of Co_3O_4. Substitution of Co by the larger Mn leads to an expansion of the unit cell, explaining the decrease in the Bragg angles of the Co_3O_4 reflections. The decrease in the intensity of the main diffraction lines is most likely due to the lower atomic scattering factor of Mn. Therefore, XRD analysis demonstrates the incorporation of Mn in the Co oxide precursor.

Table 1
Characterization of CoMn/Si catalysts.

Sample	Co (wt%)	Mn (wt%)	Mn/Co ratio	d_{XRD} Co_3O_4 (nm)[1]	d_{XRD} Co metal (nm)[2]	TEM Co (nm)	H_2 chem. (mmol/g)
Co/Si	19.2	0	0	14.6	11.0	12.6 ± 4.1	0.097
CoMn(0.05)/Si	18.8	0.95	0.05	10.1	7.6	nd	0.086
CoMn(0.1)/Si	17.4	1.68	0.1	10.8	8.1	11.9 ± 2.7	0.055
CoMn(0.25)/Si	16.3	3.85	0.25	9.9	7.4	nd	0.042

[1] particle size as determined by the Scherrer equation of the (3 1 1) reflection.
[2] estimated metal particle size after reduction, derived from the Co_3O_4 particle size by multiplication with 0.75.

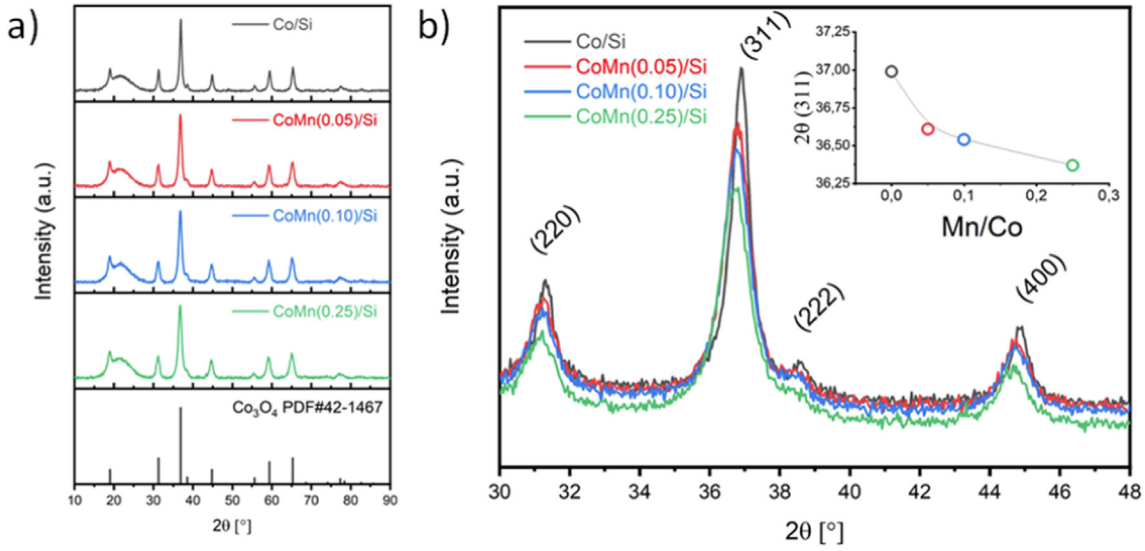

Fig. 1. (a) XRD patterns of calcined Co/Si and CoMn/Si catalysts, (b) detail of the XRD reflections between 2θ = 30 and 48° (the inset shows the peak position of the (3 1 1) reflection of Co_3O_4 as a function of the Mn/Co ratio).

H_2 chemisorption was used to compare the available surface area of metallic Co after reduction. The data in Table 1 show that the amount of chemisorbed H_2 strongly decreases with Mn content. As the particle sizes do not differ much, this decrease can, in accordance with earlier studies [12,18,34], be assigned to partial coverage by oxidic Mn species of a Co surface, which is metallic despite the use a mild prereduction treatment.

The reduction behavior of the catalysts was studied by H_2-TPR (Fig. 2). Two distinct peaks observed at 303 °C and 371 °C can be assigned to the sequential reduction steps of Co_3O_4 to CoO and of CoO to metallic Co. The initial reduction of Co_3O_4 to CoO is only slightly affected by Mn addition, while the subsequent reduction form CoO to Co^0 is delayed from 371 °C to 465 °C. This implies that the initial reduction of the spinel Co_3O_4 structure is hardly influenced by the incorporation of Mn, but that the last reduction step of CoO to metallic cobalt is strongly hindered by the presence of Mn, indicating a strong interaction between manganese oxide and cobalt after the spinel structure has ceased to exist.

The structural evolution of the Co/Si and CoMn(0.1)/Si samples during reduction was monitored by *in situ* XRD (Fig. 3). Consistent with the TPR results, the reduction of Co_3O_4 proceeds in two steps via an intermediate CoO phase. The onset of Co_3O_4 reduction is just above 200 °C. The resulting CoO phase of Co/Si is reduced at a lower temperature than CoO in the Mn-containing sample, which is in agreement with the TPR results. XRD also shows that metallic Co is already present after reduction at 275 °C with a slight delay for the CoMn(0.1)/Si sample. The differences in temperature values between Figs. 2 and 3 are caused by the use of another setup and heating rate. Analysis of the XRD patterns obtained after reduction at 450 °C indicates that the metallic Co nanoparticles consist of both fcc and hcp crystal structures with the former dominating. The hcp/fcc ratio can have a substantial impact on the catalytic performance of Co nanoparticles with hcp Co being more active than fcc Co [35]. Although it has been observed that unusual bcc phases can be formed in the presence of Mn [36] and that Mn can influence the fcc/hcp ratio, the XRD patterns of the reduced catalysts (Fig. 3) do not evidence the formation of a bcc phase nor a substantial difference in the hcp/fcc ratio by Mn addition. The main influence of Mn thus appears to be a slower reduction of CoO to metallic Co, likely by the presence of a double Mn-Co-oxide in the precursor. It has been reported that such double oxides reduce at a higher temperature than Co-oxide or a physical mixture of Mn- and Co-oxide [37].

Fig. 4 shows the Co 2p XPS spectra for Co/Si and CoMn(0.1)/Si before and after reduction at 450 °C. Reduction was done in the pretreatment chamber directly connected to the XPS analysis chamber, permitting *quasi in situ* XPS characterization. The spectra of the calcined precursors contain contributions of Co^{2+} and Co^{3+} at 781.4 and 779.6 eV, respectively. This assignment is supported by the presence of satellite features characteristic for Co_3O_4.[38] The presence of Mn decreases the Co^{2+} peak intensity of CoMn(0.1)/Si compared to the Mn-free sample. The Co^{3+}/Co^{2+} ratio increases from 2.2 for the Co/Si to 3.5 for the CoMn(0.1)/Si sample, which indicates a preferential substitution of Co^{2+} by Mn^{2+} ions in the mixed oxide spinel structure. After reduction at 450 °C for 8 h, the XPS spectra are dominated by a feature at 778.1 eV assigned to Co^0, suggesting a nearly complete reduction of Co for both samples.

The oxidation state Mn was also investigated by XPS. The Mn 2p and Mn 3s XPS spectra of the calcined as well as reduced Co/Si and CoMn(0.1)/Si catalysts are given in the Supporting Information (Fig. S2). Both spectra are dominated by satellite features

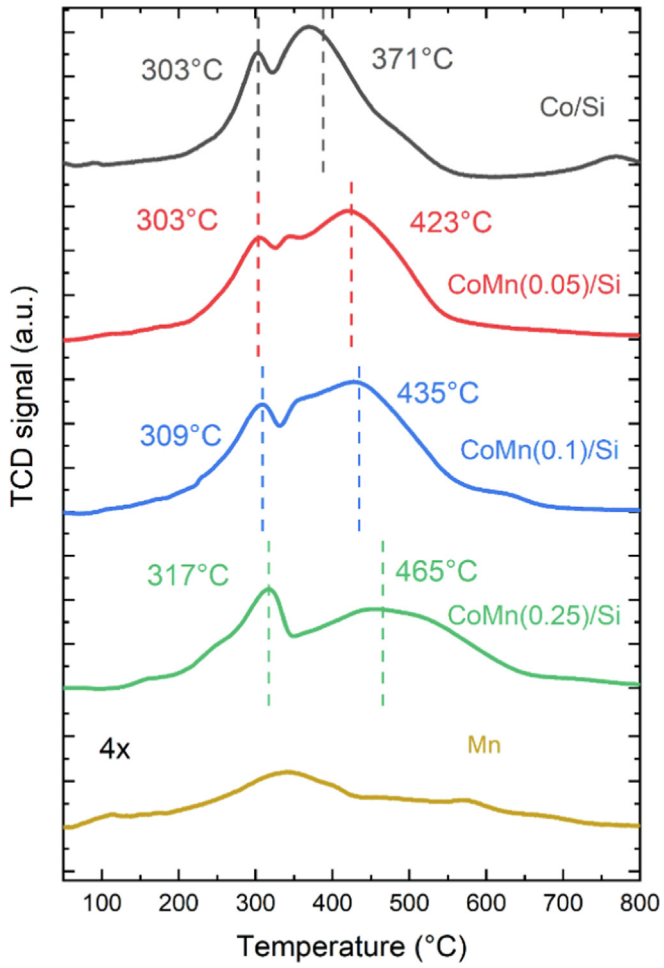

Fig. 2. H_2-TPR of Co/Si and CoMn/Si catalysts with silica supported Mn oxide as reference (1.5 wt% Mn on SiO_2).

characteristic for MnO, which are typically absent for Mn_2O_3 and MnO_2 [38]. Resolving the Mn oxidation state from the Mn 2p core line is challenging due to overlapping features at similar binding energies [38]. Instead, analysis of the Mn 3s XPS spectra can provide insight into the Mn oxidation state. The splitting of the Mn 3s core line in these spectra originates from the exchange coupling of 3s holes and 3d electrons of Mn [39]. Typical reported splitting values are 4.5–4.8 eV for MnO_2, 5.3 to 5.4 eV for Mn_2O_3, 5.5 to 5.6 eV for Mn_3O_4, and 5.6 to 5.8 eV for MnO [40,41,42]. Comparison of the Mn 3s peak splitting values of CoMn(0.1)/Si before and after reduction at 450 °C shows that Mn is reduced from Mn^{3+} (3s splitting of 5.0 eV) to Mn^{2+} (3s splitting of 5.8 eV). Finally, it is worthwhile to note that the Mn/Co ratio after reduction (0.98) is higher than before reduction (0.57), indicating an increased presence of Mn at the surface. It can thus be inferred that Mn migrates from the oxide precursor to the surface of the metallic Co particles as MnO. The presence of MnO at the surface of reduced Co nanoparticles has been reported before [9]. Based on the XPS analysis, it cannot be determined on which kind of surface structure the MnO is located. However, as chain growth still occurs after Mn addition (see below), it is unlikely that MnO is located on stepped sites, which catalyze chain growth.

3.2. Catalytic performance measurements

The influence of Mn on the Co catalyst performance was evaluated using typical industrial conditions, i.e., 20 bar, 220 °C, and a H_2/CO ratio of 2. The reaction rate, product distribution, ASF plots, and olefins-to-paraffins (O/P) ratios as a function of increasing Mn content are shown in Fig. 5. Notably, the Co-weight-based activity decreases with increasing Mn content, while the TOF based on H_2 chemisorption remains relatively constant especially above Mn/Co = 0.05. Since the site-normalized activity is constant, the decrease in the weight-based activity can most likely be ascribed to a decrease in the active surface area due to decoration of the surface by MnO. The product selectivities of the remaining Co surface is influenced significantly by Mn addition. The product distribution data show that, under these conditions, Mn addition results in an increase in the C_2-C_4 hydrocarbons selectivity from 7.7% for Mn/Co = 0 to a maximum of 29.1% for Co/Mn = 0.1 (Fig. 5b). At higher Mn/Co values, a small decrease in the light hydrocarbon selectivity is observed. The CH_4 selectivity decreases slightly and monotonously from 8.8% for Mn/Co = 0 to 7.3% for Mn/Co = 0.25. The increased selectivity to C_2-C_4 hydrocarbons goes at the expense of C_{5+} formation (from 83.5% to 60.0 %). These differences are also reflected in the ASF plots. Whereas the unpromoted sample follows the typical ASF distribution with a CH_4 selectivity higher than predicted by the ASF plot, Mn addition leads to a lower than predicted CH_4 selectivity. This is clearly due to a significant decrease in the chain-growth probability, at almost constant CH_4 selectivity. In parallel, Mn addition also increases the O/P ratio already at low Mn/CO ratios (Fig. 5d).

It is worthwhile to compare these data with performance data published earlier for Mn-promoted catalysts. Especially early studies by Hutchings et al. emphasized exceptionally high alkene, in particular propylene, yields [43,44,45] (up to 20 wt%), in conjunction with an improved activity and stability upon addition of relatively large amounts of Mn (Mn/Co > 1). Also patent literature from ExxonMobil reported CoMn catalysts exhibiting a high C_2-C_4 selectivity of 26% with a total C_2-C_4 olefins content of 83%.[46] Zong et al. [19] linked the increased light olefins selectivity to the formation of Co_2C in the presence of Mn. Yet, the CO_2 selectivity was close to 50% in their study. The CO_2 selectivity in the present study is less than 1%, which is typical for metallic Co catalysts. Furthermore, *in situ* XRD (SI, Fig. S3) data shows very limited signs of Co_2C formation, ruling out any dominant role of carburized Co. The data obtained at 20 bar and presented in Fig. 5 clearly show that Mn promotion suppresses the coupling of the chain-growth monomers (CH_x) as well as olefin hydrogenation. Decreased chain growth and suppressed hydrogenation of olefins might be a result of an increased surface coverage due to the presence of Mn, hindering olefin re-adsorption and possibly monomer coupling. To verify this hypothesis, the role of surface coverages was investigated further by studying the pressure dependence of the catalytic performance of both the promoted and unpromoted catalysts. Since pressure is also expected to influence the surface coverages. The catalyst with an Mn/Co ratio of 0.1 was chosen as representative for the Mn-promoted catalysts, as it exhibits the largest influence of Mn promotion on the Co catalyst performance, not only at high pressure (see Fig. 5 above) but also at low pressure (see Fig. 7 below). The influence of the studied pressure dependence is shown in Fig. 6.

It appears that the presence of Mn strongly influences the pressure depends of the catalytic performance. As mentioned in the introduction, earlier catalytic tests at elevated pressure contradict each other regarding the influence on the O/P ratio and the selectivities to either C_{5+} or CH_4 [7–13]. As a consequence, the product distribution data reported here for high pressure cannot be in agreement with all literature. However, the unpromoted catalyst behaves in good keeping with most reports, since the rate and TOF increase with increasing pressure (see Fig. 6a) [18,47,48]. Typically, reaction orders with respect to CO and H_2 for Co catalysts are slightly negative and close to unity, respectively [18,49,51]. This

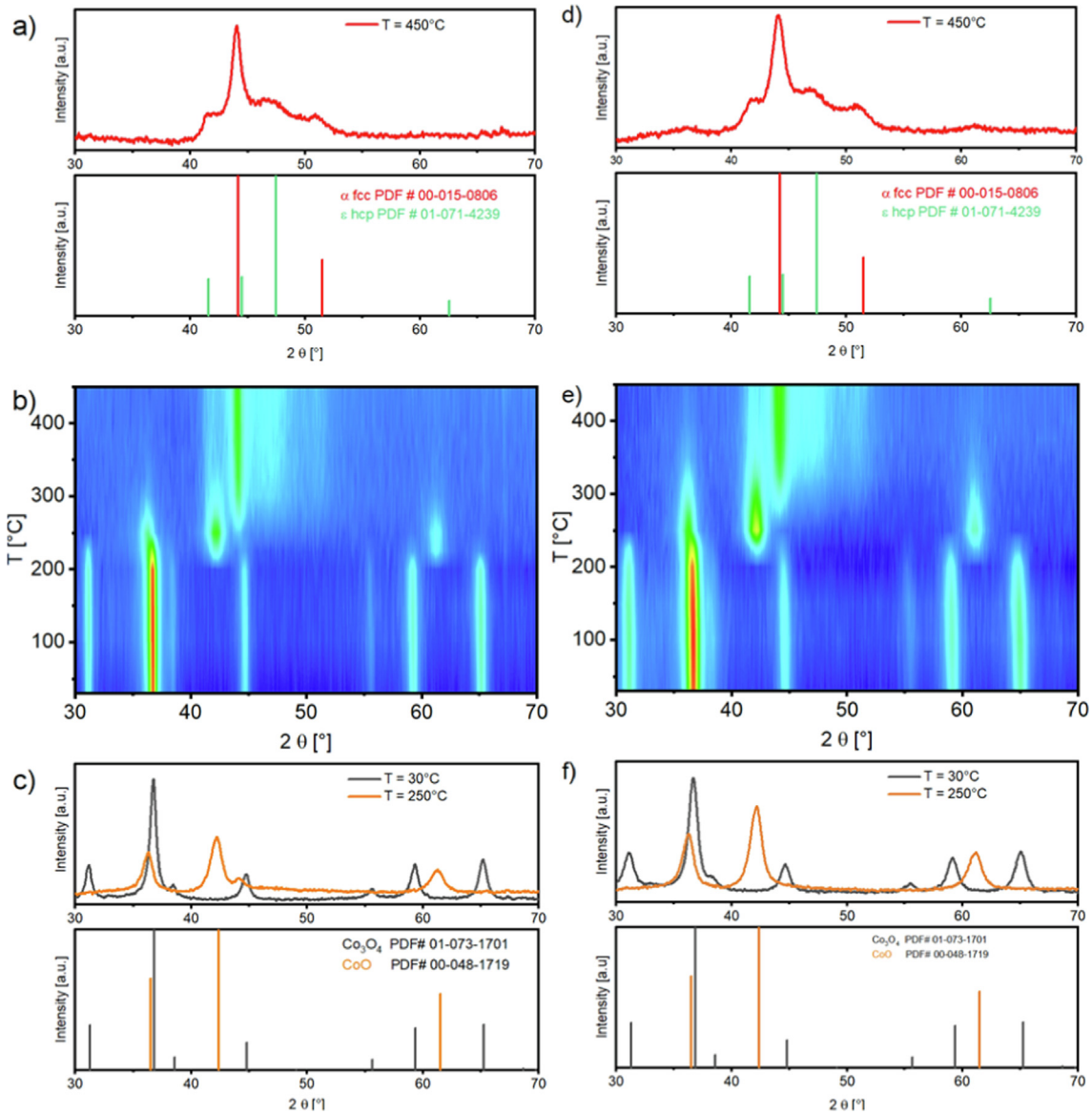

Fig. 3. *In situ* XRD during the reduction of Co/Si (left panels) and CoMn(0.1)/Si (right panels); (a) and (d) *In situ* XRD after reduction at 450 °C. The reference spectra of hcp and fcc Co are included. (b) and (e) heat plots of *In situ* XRD patterns as a function of temperature. (c) and (f) XRD patterns after reduction at 30 and 250 °C. Reference spectra of hcp and fcc Co, CoO, and Co_3O_4 are included.

results in an overall increase in reaction rate with increasing total pressure at constant H_2/CO. The selectivities of the unpromoted catalyst also behave as anticipated: at increasing pressure an increasing monomer coverage is expected, which results in a higher C_{5+} selectivity (Fig. 6c) and lower selectivity to CH_4 and C_2-C_4 products (Fig. 6b). However, in contrast to the unpromoted Co, the Mn-promoted catalyst has surprisingly a maximum in both the rate and the TOF at around 4 bar. Above this pressure, there is no clear increase (Fig. 6a). The Mn-promoted catalyst follows at increasing pressure the same trends in product distribution as the unpromoted one, but reaches a maximum C_{5+} selectivity at about 4 bar and a minimum for the C_2-C_4 selectivity at the same pressure (Fig. 6c). Only the CH_4 selectivity decreases with increasing pressure for both catalysts (Fig. 6b), although the influence of Mn promotion on the CH_4 selectivity diminishes with increasing pressure. Understandably, the C_{5+} selectivity selectivity mirrors the selectivity to the other hydrocarbons CH_4 and C_2-C_4 for both catalysts. Notably, at low pressure, the Mn-promoted catalyst has a higher C_{5+} selectivity and a lower C_2-C_4 selectivity than the unpromoted catalyst. However, an almost opposite selectivity distribution is observed at 20 bar, when the Mn-promoted catalyst has a lower C_{5+} selectivity and a higher C_2-C_4 selectivity. The turning point from one selectivity being higher than the other occurs around 4 bar. Fig. 6c also shows that over the whole pressure range Mn promotion increases the olefin to paraffin ratio of the C_3 hydrocarbons. It can thus be concluded that an increase in total pressure for the unpromoted catalyst leads to a similar effect as an increase in Mn content at low pressure, i.e., an increased activity, C_{5+} selectivity, and O/P ratio. These two similar effects can tentatively be explained in a the same way: Mn promotion as well as an increased pressure enhance the coverage of surface species, hindering hydrogenation of olefins by re-adsorption and increasing the coupling probability of growth monomers. In order to determine the role of the surface adsorbed layer on the selectivity trends, the surface coverages were measured by steady-state isotopic transient kinetic analysis (SSITKA) experiments.

SSITKA was carried out at model FT conditions, viz. at 220 °C and a total pressure of 1.85 bar with a H_2/CO ratio of 3. The

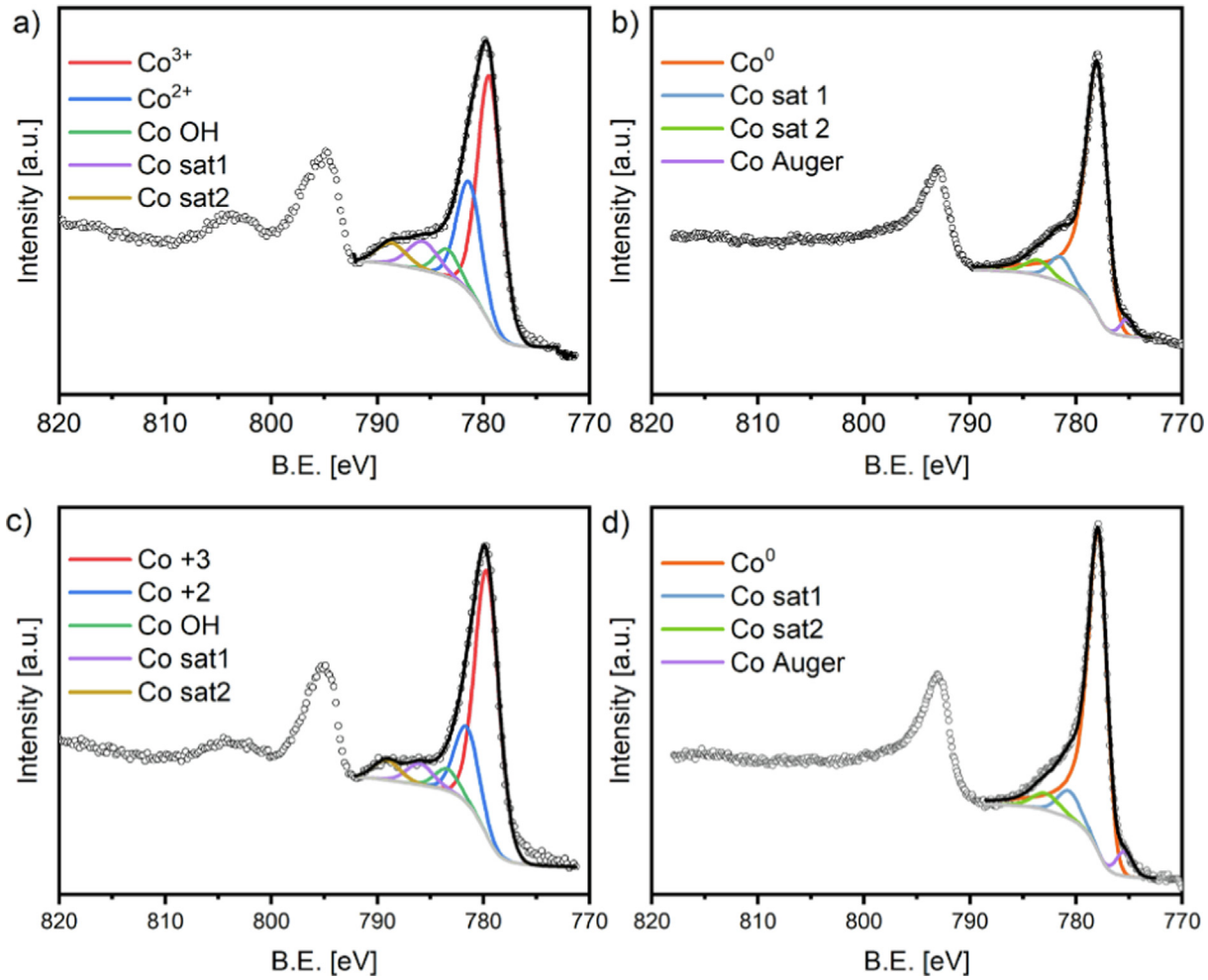

Fig. 4. *Quasi in situ* XPS spectra of the Co 2p region of calcined and reduced (450 °C) catalysts: (a) calcined Co/Si, (b) reduced Co/Si, (c) calcined CoMn(0.1)/Si, and (d) reduced CoMn(0.1)/Si.

steady-state catalytic performance of the catalysts under these conditions is displayed in Fig. 7, showing an overall beneficial influence of Mn on the CO conversion. TOF, C_{5+} selectivity, and chain-growth probability. Simultaneously, the CH_4 and C_2-C_4 selectivity decrease with increasing Mn content. The changes in selectivities and activity upon Mn addition to Co is almost reversed to those observed at 20 bar (Fig. 5), as expected from the pressure dependency of the promotional effect of Mn (Fig. 6). Notably, in both cases the largest effect of Mn addition occurs at an Mn/Co ratio of 0.1. This has also been described before in literature [17,18,34], where it was explained by two counterbalancing effects. On one hand, Mn enhances the FT reaction rate on Co. On the other hand, Mn, which is by itself catalytically inactive, blocks the catalytic cobalt sites. At too high Mn/Co ratios, the latter effect appears to be dominant.

The residence times τ and surface coverages θ of CO and CH_x determined under the same conditions as the experiments presented in Fig. 7 are depicted in Fig. 8a as a function of the Mn/Co ratio. τ_{CO} is practically independent of the Mn content, while τ_{CH_x} increases with increasing Mn/Co ratio. The coverages of CO and CH_x species increase with increasing Mn content. A higher coverage of CH_x is expected to lead to a higher chain-growth probability. This is in line with the increasing C_{5+} selectivity (Fig. 7a) and with the increasing difference between TOF_{CO} and TOF_{CH4} at higher Mn/Co ratio (Fig. 7b), as this difference represents the rate of carbon conversion to C_{2+} hydrocarbons. Notably, although Fig. 7a shows that, above the Mn/Co ratio of 0.1, the C_{5+} selectivity increases, the calculated chain-growth probability does not increase. The extreme increase in CH_x coverage leads thus to the formation of heavy hydrocarbons that are not included in the calculation of the chain-growth probability in our work (namely C_3 to C_7).

Noteworthy is the increasing CO surface coverage with increasing Mn/Co ratio. Chen et al. determined by SSITKA that the CO coverage on (unpromoted) Co/SiO_2 can be as high as 0.4[23], just as we observe here for the samples up to an Mn/Co ratio of 0.1. From a theoretical perspective, the maximum attainable CO coverage on Co(0001) is 7/12 (0.58) [50]. However, at an Mn/Co ratio of 0.25, the CO coverage is as high as 0.67, indicating that an exceptionally high coverage can be obtained in the presence of Mn. Apparently, Mn enhances CO adsorption. In contrast to unpromoted cobalt catalysts, this adsorbed CO does not hinder CO dissociation. Hindrance of CO dissociation by co-adsorbed CO is often used to explain the negative order in CO for Co catalysts. As can be seen in Fig. 8b, the reaction order with respect to CO is indeed negative for unpromoted but positive for Mn promoted Co. The change in CO reaction order from negative to positive through Mn promotion suggests that, in the presence of Mn, CO dissociation does not need vacancies on the metallic cobalt surface. It can thus be speculated that CO adsorption and dissociation take place on Mn-promoted cobalt sites. This aspect is investigated further with IR spectroscopy and density functional theory calculations. Most impor-

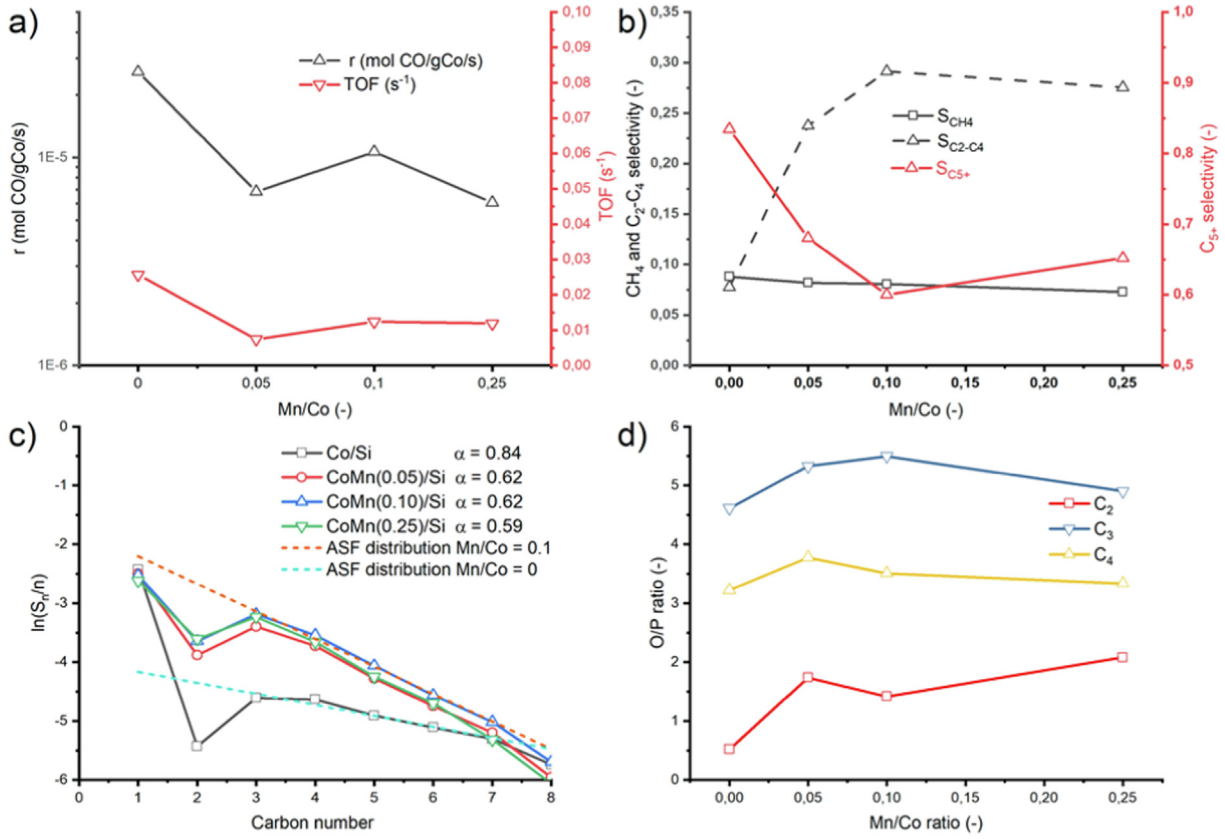

Fig. 5. Catalytic performance of reduced Co/Si and CoMn/Si catalysts as a function of Mn/Co ratio (p = 20 bar, T = 220 °C, H_2/CO = 2): (a) Reaction rate (mol CO/gCo) and TOF (s^{-1}); (b) CH_4, C_2-C_4 and C_{5+} selectivity; (c) Anderson-Schulz-Flory (ASF) plot; (d) O/P ratios for C_2, C_3 and C_4.

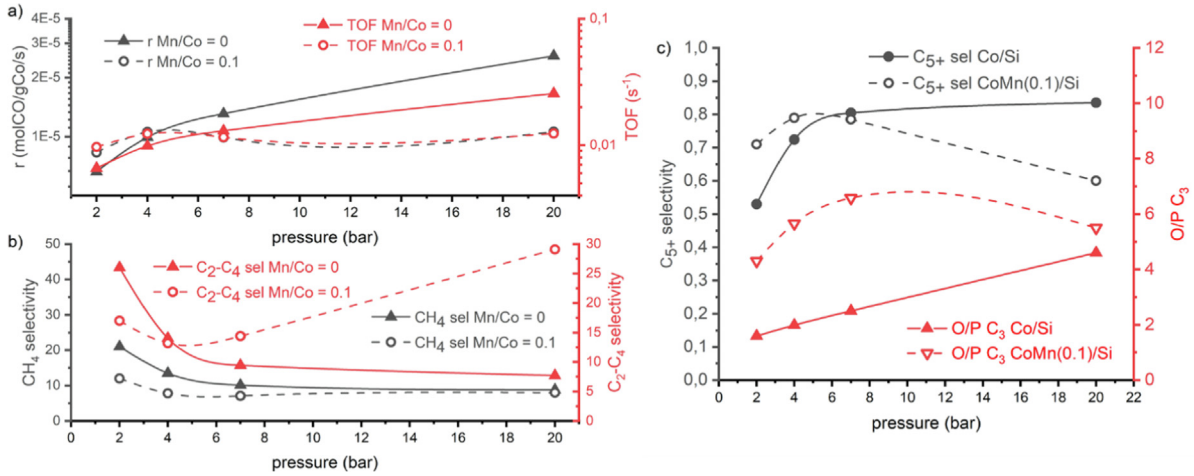

Fig. 6. (a) Reaction rate (mol $CO/g_{Co}/s$) and TOF (s^{-1}) (b) CH_4 and C_2-C_4 hydrocarbons selectivity (c) C_{5+} selectivity and olefin to paraffin ratio of C_3 (O/P_3) for Mn/Co = 0 (triangle) and Mn/Co = 0.1 (circle) as a function of total pressure. Conditions: T = 220 °C, H_2/CO = 2, and p_{total} = 2, 4, 7, or 20 bar.

tantly, it is evident from Fig. 8a that the presence of Mn leads to a higher coverage of CH_x, despite the increasing CO coverage. A higher CH_x coverage explains the above described effects of Mn promotion at low pressure. Since a higher monomer coverage not only leads to a higher coupling rate at the expense of CH_4 formation, but also, in combination with the high CO coverage to less readsorption of olefins. Hence, these SSITKA results explain the appearance of longer chain products and a higher O/P ratio for Mn-promoted catalysts.

3.3. IR spectroscopy

IR spectroscopy was carried out to understand better the impact of Mn on the adsorption and CO dissociation activity. In one set of measurements, IR spectra were recorded with increasing CO coverage (0 – 10 mbar CO) at room temperature, followed by ramping the temperature to 300 °C. A second set of IR measurements was carried out *in situ* under a synthesis gas atmosphere (H_2/CO = 2), whilst ramping the temperature to 300 °C.

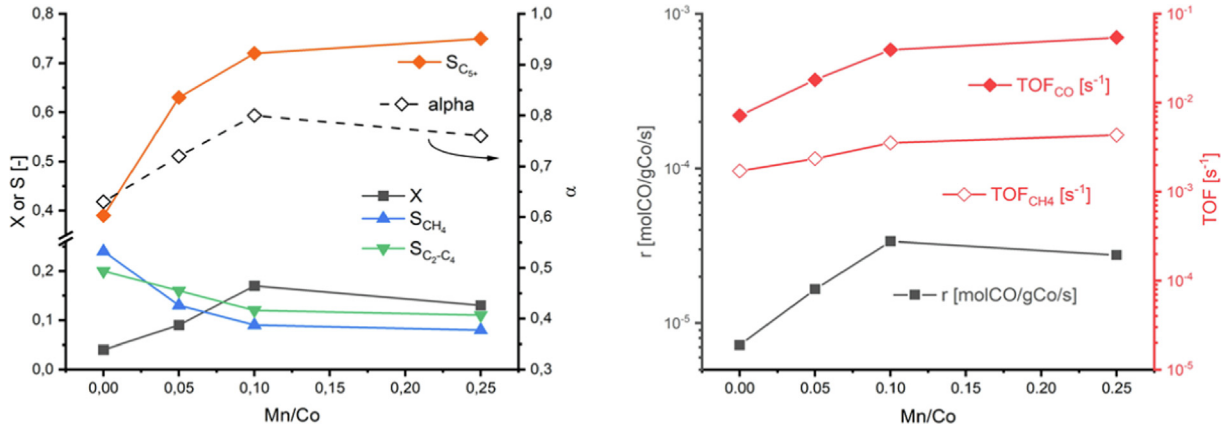

Fig. 7. (left: CH_4 selectivity (blue up triangles), C_2-C_4 hydrocarbons selectivity green down triangles), C_{5+} selectivity (red diamonds), chain-growth probability alpha based on the C_3 to C_7 hydrocarbons (open diamonds) CO_2 selectivity (circles), and conversion (X) as a function of the Mn/Co ratio. (right) TOF_{CO} and TOF_{CH4} and the Co-based reaction rate as a function of Mn/Co ratio. Conditions: T = 220 °C, H_2/CO = 3, p_{total} = 1.85 bar. The chain growth. (For interpretation of the references to colour in this figure legend, the reader is referred to the web version of this article.)

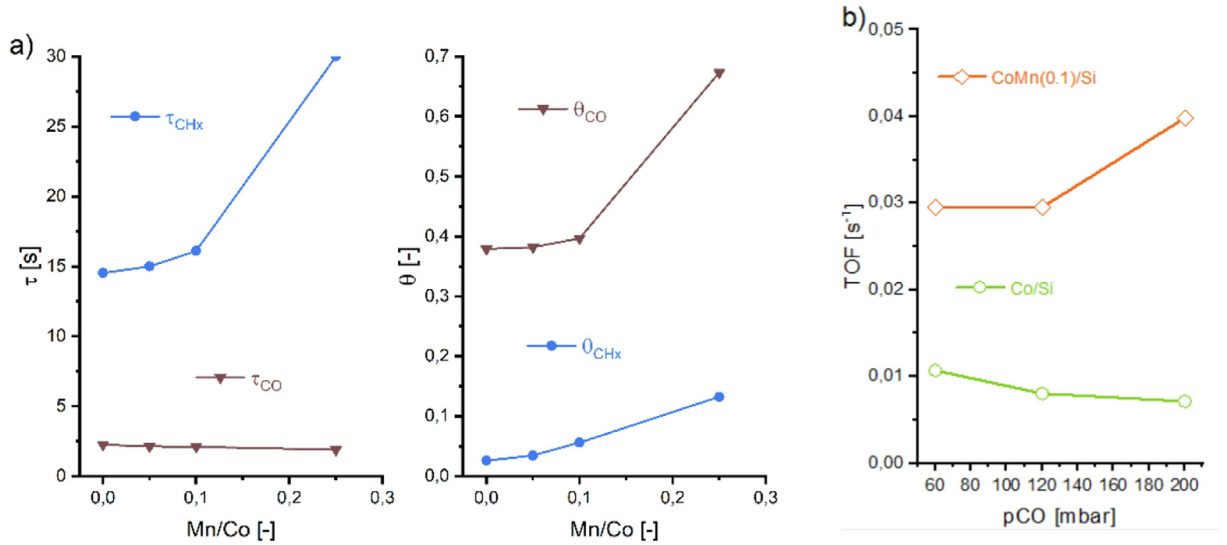

Fig. 8. (a) Residence time τ of CO (triangle down) and CH_x (circle) and surface coverage θ of CH_x (circle) CO (triangle down) as a function of the Mn/Co ratio. (b) TOF as a function of CO partial pressure for unpromoted (circle) and Mn/Co = 0.1 (circle) catalysts. Conditions: T = 220 °C, total pressure = 1.85 bar, p_{H2} = 600 mbar, p_{CO} = 200 mbar.

The CO IR spectra recorded at room temperature with increasing CO partial pressure (Fig. 9) are typical for CO adsorption on Co nanoparticles [51]. The bands at 2020 cm^{-1}, 1935 cm^{-1} and 1835 cm^{-1} can respectively be ascribed to linear (top), two-fold (bridged) and threefold (hollow) adsorbed CO on extended Co surfaces [52,53]. The blue-shift of the IR band of top-adsorbed CO with increasing coverage can be attributed to lateral interactions. For instance, Weststrate et al. [53] showed that, up to a CO coverage of around 0.15 ML, the top-CO stretching frequency and the IR intensity increased linearly, leveling off when approaching a coverage of 0.33 ML.[54] DFT calculations support this interpretation [54]. The corresponding spectra for the Mn-promoted catalysts are qualitatively similar. The most obvious changes upon Mn addition are the lower intensity at low CO pressure of the CO adsorption bands, in line with the decreasing metal surface by Mn addition as observed by H_2 chemisorption. The presence of Mn also leads to a loss of three-fold CO adsorption sites. This was also observed by Den Breejen et al. [34] The CO IR spectra of the Mn-promoted catalysts also contain a feature at 1650 cm^{-1}, which becomes more intense with increasing CO coverage. This band, which is stronger at higher Mn/Co ratios, can be assigned to a CO_3^{2-} stretching vibration. Such carbonates can originate from the reaction of CO or CO_2 with metal oxides such as MnO [55]. Although we cannot exclude that the carbonates are formed by CO interacting with MnO, it is likely that they are formed by interaction with CO_2, which would imply that CO can react on the catalyst via the Boudouard reaction to surface C species and CO_2.

A temperature-programmed IR experiment at a CO partial pressure of 10 mbar leads to pronounced changes of the IR spectra (Fig. 10). The CO IR spectra for the Co/Si catalyst are very similar to those reported by Chen et al. [51] The small red-shift of top-adsorbed CO towards slightly lower wavenumbers during heating to 150 °C can be explained by desorption of CO, resulting in less lateral interactions. The clear blue-shift from 2022 cm^{-1} to 2068 cm^{-1} observed in the 150 to 175 °C temperature range, which goes together with a strong increase of the IR intensity can be explained by the formation of co-adsorbed C and O. Model experiments by Chen et al.[51] DFT calculations showed that the presence of co-adsorbed C and O leads to a blue-shift of the CO band in parallel with an increase in the extinction coefficient. A similar shift has been described in literature and coupled to the presence of co-adsorbed O or C [51,52]. The blue-shift occurring during

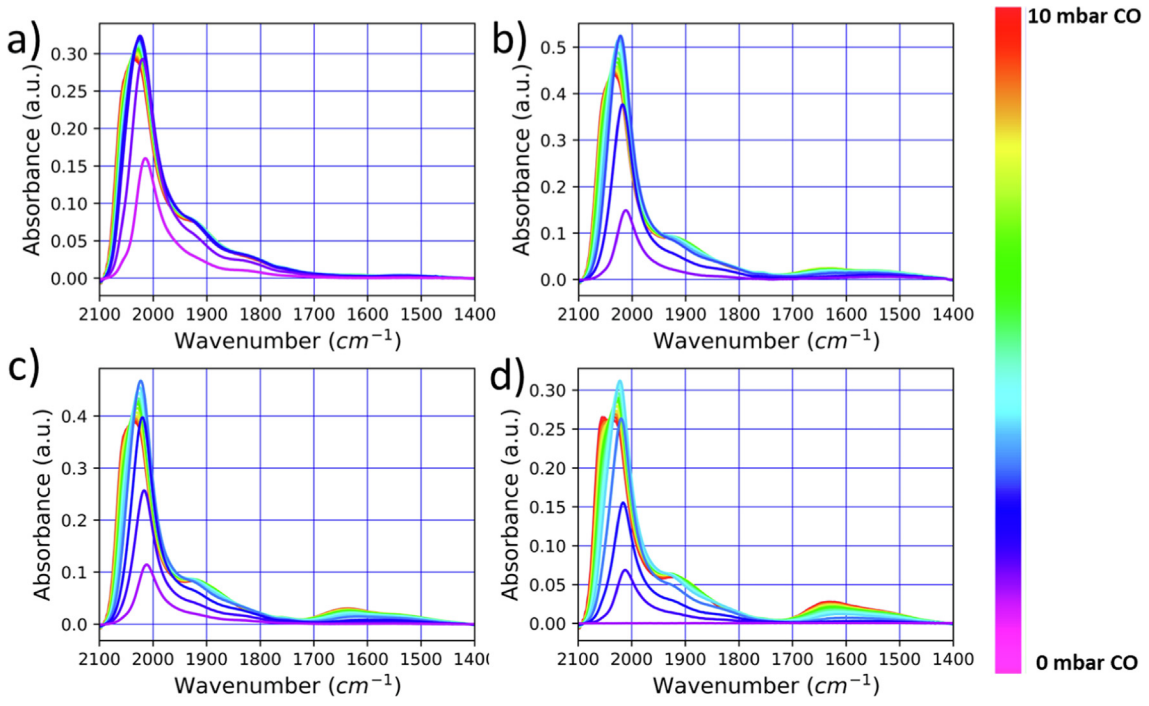

Fig. 9. CO IR spectra at 20 °C, p_{CO} = 0 to 10 mbar. (a) Co/Si; (b) CoMn(0.05)/Si; (c) CoMn(0.1)/Si; (d) CoMn(0.25)/Si.

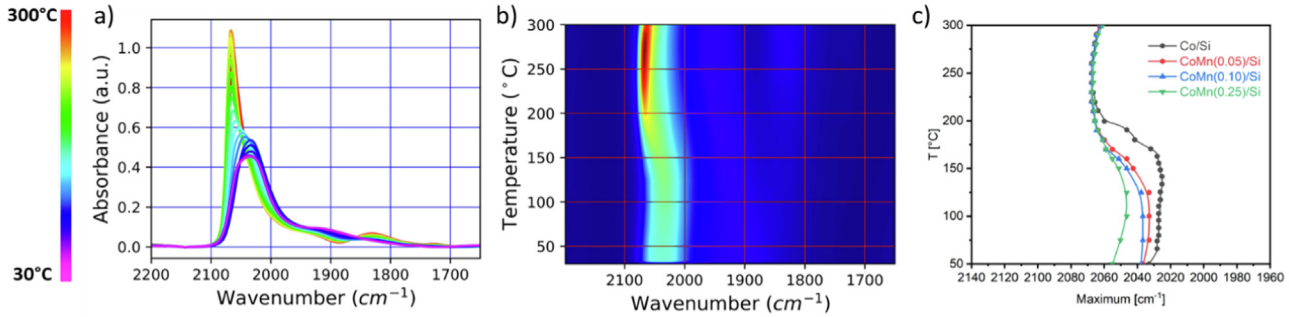

Fig. 10. Temperature-programmed IR spectra of CO (a), Co/Si IR spectrum as a function of temperature (45–300 °C) at an initial CO partial pressure of 10 mbar (b), Co/Si heat map of IR spectra in the 2200–1650 cm^{-1} range (colors indicate IR intensity (a.u.) which increases from violet to red). (c) position of the peak maximum of linear CO as a function of temperature and the Mn content. (For interpretation of the references to colour in this figure legend, the reader is referred to the web version of this article.)

the temperature-programmed IR spectroscopy can thus be linked to CO dissociation, yielding co-adsorbed C and O. Comparison of the shift on Co/Si (Fig. 9b) with the shift on CoMn(0.1)/Si (Fig. 10d) shows that Mn addition lowers the onset temperature of the blue-shift by nearly 50 °C (from 175 °C to 125 °C) indicating that CO dissociation is facilitated by the presence of Mn. The blue-shift occurs for all CoMn/Si samples (Fig. 10e). In order to determine whether this enhanced CO dissociation upon Mn addition also occurs under reaction conditions, the above experiments were repeated in a synthesis gas atmosphere (H_2/CO = 2, p_{total} = 100-mbar). An overview of the results is shown in Fig. 11.

Fig. 11a and 11b show the IR spectra for CoMn(0.1)/Si as a function of the temperature. In contrast to the conditions in Fig. 10, the surface contains also hydrogen. In the presence of hydrogen, the position of linearly adsorbed CO at room temperature is shifted from 2020 cm^{-1} to 2050 cm^{-1}, which is most likely due to lateral interactions with hydrogen-containing reaction intermediates. Similar to Fig. 10, a blue-shift due to CO dissociation, is observed. The temperature at which the blue-shift occurs is lower in synthesis gas than in a CO atmosphere. The influence of Mn on the onset of the blue-shift is less pronounced than in the presence of hydrogen.

Fig. 11d depicts the C–H stretch region of hydrocarbons for the Co/Si and CoMn/Si catalysts. The spectra are dominated by the absorption bands of gas-phase CH_4. Above 150 °C, all catalysts show distinct vibrations in the range of 2900 to 3200 cm^{-1} typical for gaseous CH_4 and located on the low- and high-frequency side of the ν_3 C–H stretch vibration at 3020 cm^{-1}. The typical vibrations of gas-phase CH_4 appear at approximately 190 °C independent of the catalyst. A high CH_4 selectivity for cobalt catalysts is as expected under the low total pressure (100 mbar) conditions with a high H_2/CO ratio of 3. The weaker and broader features in the 2800 – 3000 cm^{-1} regime are typical for hydrocarbons with C–C bonds. Notably, the spectra for Co/Si contain only bands for CH_4, while the Mn-containing catalysts also exhibit bands due to higher hydrocarbons as evidenced by the sp^3 C–H vibrations of CH_2 and CH_3 in the 2800–3000 cm^{-1} range (CH_2 at 2927 cm^{-1} and 2864 cm^{-1} and CH_3 at 2968 cm^{-1}). This indicates that Mn facilitates the formation of higher hydrocarbons as compared to Co/Si. These bands appear already at a relatively low temperature, i.e.,

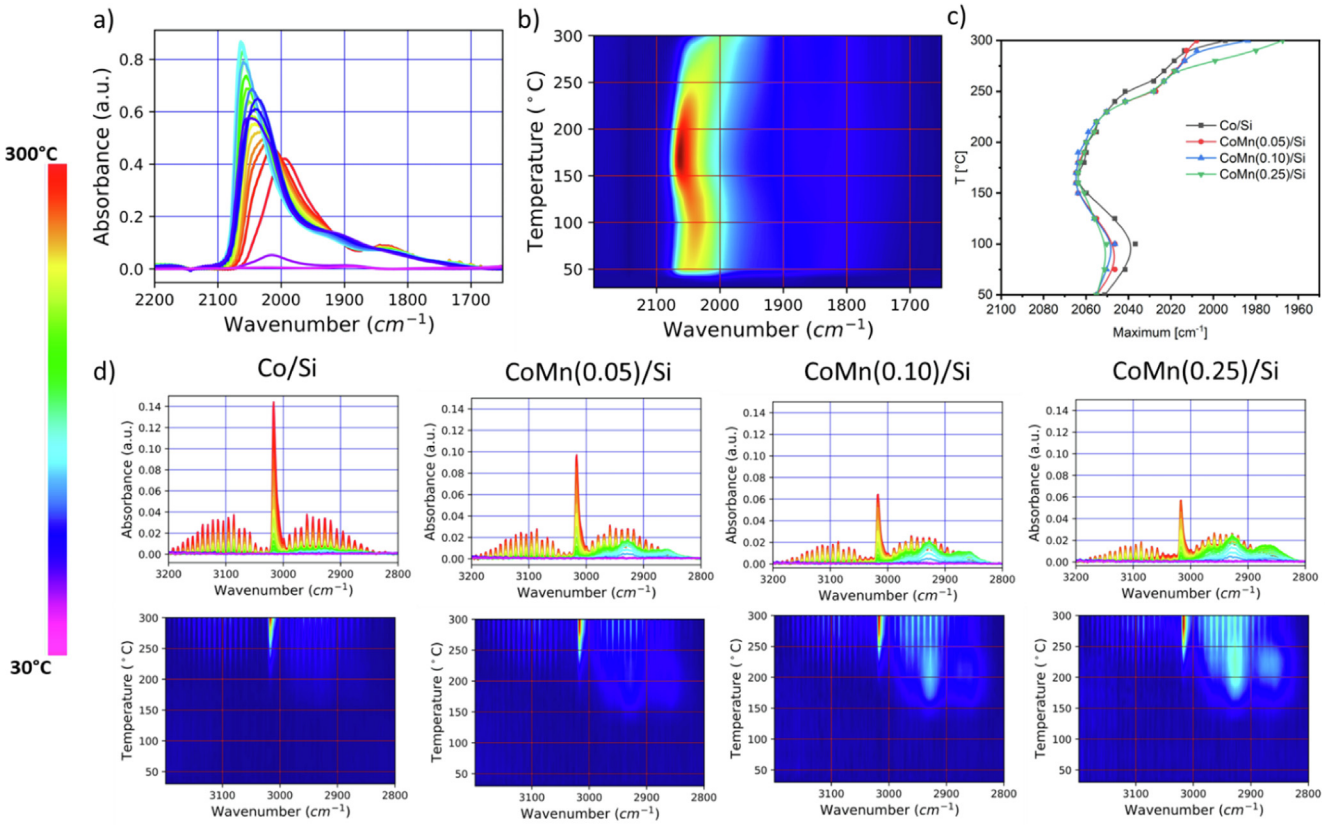

Fig. 11. Temperature-programmed *in situ* IR spectroscopy in synthesis gas (H_2/CO = 2, p_{total} = 100 mbar) (a), (b) CO stretch region as a function of temperature for CoMn(0.1)/Si. Colors in heat map (b) indicate IR intensity (a.u.) which increases from violet to red. (c) plot of the position of the peak maximum of linear CO as a function of temperature and Mn content. (d) 3200–2800 cm^{-1} region representing hydrocarbon C–H stretch vibrations during temperature-programmed reaction in synthesis gas for Co/Si and CoMn/Si catalysts and the corresponding heat maps in which the colors indicate IR intensity (a.u.) which increases from violet to red. (For interpretation of the references to colour in this figure legend, the reader is referred to the web version of this article.)

just below 150 °C. The CH_2 and CH_3 bands are most intense in the 200–220 °C range. We speculate that the observed hydrocarbon bands stem from adsorbed hydrocarbon fragments, which desorb or react at higher temperatures. In summary, the IR spectroscopy results show that Mn promotes the dissociation of adsorbed CO and enhances the formation of higher hydrocarbons.

3.4. Computational modeling

DFT calculations were employed to investigate how the presence of MnO on the metallic Co surface can affect CO dissociation. A relatively simple Mn_4O_4/Co(0001) model was chosen to represent MnO on a metallic Co surface. Various structures of Mn_4O_4/Co(0001) were identified by a DFT-based genetic algorithm method. The most stable structures are given in Fig. S4. In structure with the lowest energy each Mn atom binds to two surface Co atoms and two O atoms (see also Fig. 12a). This structure is very similar to the one determined for Mn_4O_4 on the Ni(1 1 1) surface by Vrijburg et al. [29] It was shown that such model structures can lower CO or CO_2 dissociation barriers via reactions involving an O vacancy in the Mn_4O_4 cluster. Here, similar pathways for CO dissociation are explored, starting from an Mn_4O_4 cluster with a vacancy, i.e., Mn_4O_3. Specifically the elementary CO dissociation step is examined, as this supposedly is the rate-limiting step in the whole Fischer-Tropsch reaction sequence. The reaction energy needed for the creation of such a vacancy was also calculated.

DFT calculations show that direct CO dissociation can occur on the step-edge sites of Co, viz. on the Co $(11\bar{2}1)$ model surface. A typical value for CO dissociation activation energy on a stepped Co $(11\bar{2}1)$ surface is 1.07 eV [35]. CO dissociation on the close-packed Co(0001) surface is very difficult with total activation barriers of 2.46 eV for direct and 1.83 eV for H-assisted CO dissociation, respectively [35]. Three pathways were explored for CO dissociation on the vacancy containing Mn_4O_3/Co(0001) model. Direct CO dissociation and H-assisted dissociation via either an HCO or COH intermediate. The corresponding the reaction energy paths are shown in Fig. 13a. The involved transition states are depicted in Fig. S5. The direct and H-assisted CO dissociation via COH have overall barriers of 1.71 eV and 1.26, respectively. The most favorable CO dissociation mechanism on Mn_4O_3/Co(0001) involves HCO as a surface intermediate with an overall barrier of 0.98 eV, which is slightly lower than the most favorable CO dissociation on unpromoted Co. Hence, these calculations show that H-assisted CO dissociation at the Co-Mn_4O_3 interface is much easier than on the planar surfaces of Co and slightly easier than on a step-edge sites of Co. The finding that H-assisted CO dissociation is favored fits with the IR experiments above, which show that the blue-shift due to CO dissociation occurs at lower temperatures in the presence of hydrogen.

The calculations above started with an Mn_4O_4 cluster in which a vacancy was created, i.e., Mn_4O_3. After CO dissociation, the oxygen of CO fills this vacancy. In order to close the catalytic cycle, the vacancy has to be created again. The activation energy for removing one oxygen should preferably be equal or lower than the above-calculated activation energies for CO dissociation. The activation energy diagrams for the creation of an O vacancy by H_2O formation at the interface of the Mn_4O_4/Co(0001) structure via two different pathways are shown in Fig. 13b and 13c. Creation

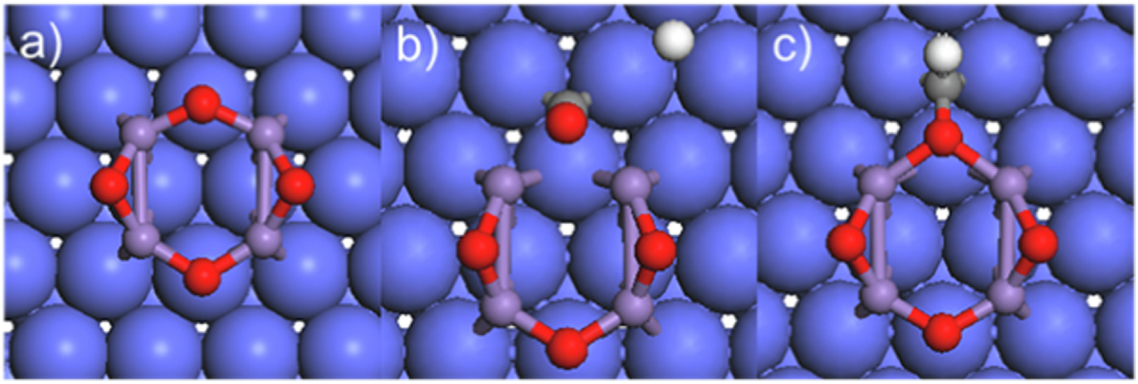

Fig. 12. (a) DFT structure of an Mn_4O_4/Co(0001) cluster, (b) configuration CO adsorbed near a on Mn_4O_3/Co cluster, (c) HCO transition state for hydrogen assisted CO dissociation. (blue: cobalt, red: manganese, grey: oxygen, white: hydrogen). (For interpretation of the references to colour in this figure legend, the reader is referred to the web version of this article.)

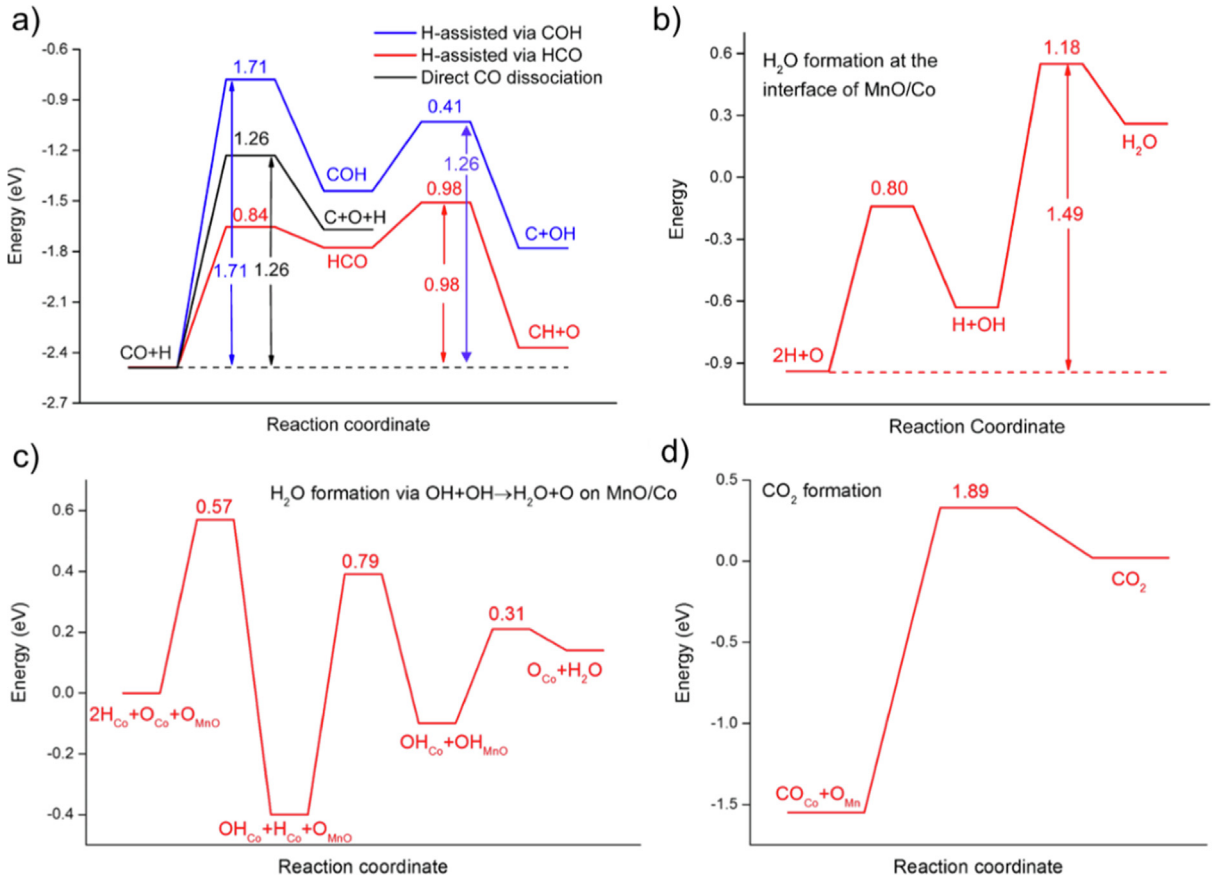

Fig. 13. (a) Potential energy diagrams based on DFT calculations for CO dissociation on a vacancy containing Mn_4O_3/Co(0001) cluster. (b), (c) DFT calculations for O vacancy formation on the Mn_4O_4/Co(0001) cluster via H_2O formation. (d) DFT calculations for O vacancy formation on the Mn4O4/Co(0001) cluster via CO_2 formation. Numbers above the lines are the energy barriers for the forward reaction from the nearest preceding stable state.

of a vacancy in an Mn_4O_4 cluster by reaction of an oxygen atom with subsequently two hydrogen atoms requires overcoming a barrier of 1.18 eV (Fig. 13b), whilst the overall barrier is 1.49 eV. In another pathway, hydrogen reacts with an oxygen atom in the cluster leading to an OH group on the Mn_4O_4 cluster, which subsequently reacts with an OH species on the Co metal. This path has a lower maximum barrier of 0.79 eV (Fig. 13c). The geometries of the corresponding transition states are shown in Fig. S6a and S7. The occurrence of OH intermediates adsorbed on Co during reaction can be expected as water is a primary product of the FT reaction. The barrier for vacancy creation of 0.79 eV is lower than for promoted CO dissociation (0.98 eV), making the highest barrier in the whole catalytic cycle 0.98 eV. For completeness, another pathway for vacancy creation, viz. via a reaction with CO to CO_2, was also computed. However, the barrier for formation of a vacancy via this pathway, which is shown in Fig. S8, is 1.89 eV (Fig. 13d), much higher than the computed barriers for CO dissociation and H_2O formation.

In summary, DFT calculations on a simple surface model show a facile pathway for the dissociation of CO by means of an O vacancy

in the MnO, which is the result of the reaction of O in MnO with hydrogen and adsorbed OH forming H_2O. The overall barrier for CO dissociation via this vacancy promoted pathway is lower than the CO dissociation barrier on step-edge sites of Co (0.98 eV versus 1.07 eV, respectively). The lower activation energy can contribute to a higher reaction rate on the Mn-promoted Co catalysts. Besides, the presence of MnO on Co can also lead to an increase in the number of active sites for CO dissociation compared to the pure metallic Co surface, which requires step-edge sites. In relation to the CO reaction orders discussed above, it can be mentioned that CO dissociation at the Co-MnO interface is not limited by CO coverage on the metal as is the case for the unpromoted Co metal surface.

4. General discussion

Physicochemical characterization of the catalyst precursor shows that Mn is completely integrated in the mixed oxide spinel catalyst precursor. The presence of the mixed oxide spinel of Co and Mn retards the reduction of Co, especially the last reduction step of CoO to metallic Co. Nonetheless, according to XPS analysis after reduction at 450 °C, Co is completely reduced to metallic Co for all Mn-promoted catalysts, while Mn is converted to MnO with Mn in the 2 + oxidation state. H_2 chemisorption and the relative Co and Mn signals in XPS indicate that the metallic surface of Co nanoparticles is decorated with MnO. The presence of MnO in close interaction with the Co surface is in agreement with previous observations [18]. Mn does not significantly affect the Co particle size. All catalysts contain Co particles of about 12 nm. The FT performance of these catalysts is thus not affected by structure sensitivity that limits the activity of Co particles smaller than 6 nm [13,56].

In the last two decades, a substantial amount of research has been devoted to study the impact of Mn promotion on the Co-catalyzed FT reaction, often with contradicting outcomes. In this study, the influence of Mn promotion on silica-supported Co was studied for the FT reaction at 220 °C and in the pressure range of 2 to 20 bar. The results indicate that the conflicting views in literature can mostly be attributed to different reaction conditions. Specifically, the total reaction pressure can significantly influence the effect of Mn promotion. At pressures below 4 bar, Mn acts as a promoter for Co in the FT reaction resulting in higher rates, turn-over frequencies and C_{5+} selectivity. However, the opposite holds at higher pressure. This stems from substantially different pressure dependence of the unpromoted and Mn-promoted Co catalysts. For the unpromoted catalyst an increase in pressure leads to a higher reaction rate and higher C_{5+} selectivity with the most pronounced increase in the 2 to 6 bar pressure range. On the other hand, for the Mn-promoted catalyst, this trend is remarkably different. Though the activity and C_{5+} selectivity also initially increase with increasing pressure, the activity stabilizes and the C_{5+} selectivity starts to decrease steeply above 4 bar. As a result of these opposite trends Mn enhances C_{5+} selectivity at low pressure, but suppresses it at high pressure. Nonetheless, Mn promotion decreases the CH_4 selectivity over the whole studied pressure range.

To explain the pressure dependence of the promotional effect of Mn, the role of pressure in the FT reaction and the mechanism of Mn promotion is discussed here. Mechanistic work of Chen et al. [23] has demonstrated that the increasing activity and C_{5+} selectivity when the reaction pressure is increased can be well explained by a higher CO coverage, which leads to a higher CH_x monomer coverage and, thus, higher activity and chain-growth probability. This clearly also holds for the unpromoted Co catalyst in this study, and for the Mn promoted catalysts up to 4 bar.

Temperature-programmed IR spectroscopy in the presence of CO shows a lower onset temperature for CO dissociation in the presence of Mn, indicating a positive role of MnO in the CO dissociation. Similar IR measurements in synthesis gas show that unpromoted Co produces under the conditions used only CH_4, but that Mn-promoted Co also forms larger hydrocarbons at a significantly lower temperature than the formation of CH_4. SSITKA carried out at a relatively low pressure confirms the positive impact of Mn on the activity and CH_x coverage. This can explain well the higher chain-growth probability in the presence of Mn, yielding more longer hydrocarbons and thus less CH_4 at low pressure.

DFT calculations using a Mn_4O_4/Co(0001) model show that CO can dissociate at the Co-MnO interface with a lower overall activation barrier than on the most active metallic Co step-edge sites. The modelled catalytic cycle involves the generation of an oxygen vacancy by removal of O from MnO as H_2O, followed by H-assisted C-O dissociation. The oxygen atom of CO replenishes the oxygen vacancy, leaving behind a CH fragment on the metallic Co. Thus, according to DFT, the decoration of Co with MnO results in the formation of additional CO dissociation sites on Co nanoparticles with a lower activation energy. The enhanced CO dissociation observed by IR and SSITKA experiments is thus in agreement with the outcome of the DFT calculations. Since Co typically operates in the monomer formation limit regime with CO dissociation being the rate-limiting step [21,57], enhanced CO dissociation by Mn promotion can explain the higher reaction rate.

A CO activation mechanism via an O vacancy in Mn oxide as modelled by DFT is in line with the concept launched by Barrault et al. that redox centers are active sites for CO dissociation [14], but seems in contradiction with the results of the group of Bell, who sees, when comparing different promoters, a direct correlation between the activity and the relative Lewis acidity of the promoter [6]. On the other hand, the Lewis acidity of a cation depends on the number of coordinating oxygen atoms [58]. It could thus be speculated that the same phenomenon of CO activation is just described by another parameter, i.e., Lewis acidity versus vacancy formation. Nonetheless, in contrast to previous literature, which only correlates activity with a specific parameter, a complete mechanistic understanding of the catalytic cycle is presented here.

Notably, the reaction order with respect to CO is negative for unpromoted cobalt as widely reported for Co-based FT catalysts [17,18], but positive for Mn-promoted Co. The negative order reflects the need of surface vacancies on the metallic Co surface for CO dissociation. The positive reaction order in CO for the Mn-promoted Co catalyst can be explained by the dissociation of CO at the Co-MnO interface. Since this mechanism does not require two neighboring vacant Co surface sites, self-poisoning by CO does not occur. This implies that at high CO coverage the reaction will mainly proceed at Co-MnO interfaces.

Increasing the Mn content in promoted Co catalysts from Mn/Co = 0 to Mn/Co = 0.25 at a reaction pressure of 20 bar results in a decreased C_{5+} selectivity and chain-growth probability, whereas the CH_4 selectivity is hardly affected. As a result, the CH_4 yield is not higher than expected from the ASF distribution as is usually the case for Co, but gets in line with the prediction of the AFS plot. The promotional effect of Mn reaches a maximum at an Mn/Co ratio of 0.1, at both low and high reaction pressures. This is in accordance with previous literature for Co on various supports [6,11,17,18,34] and has tentatively been ascribed to the formation of an optimum mixed Mn-Co-oxide crystal structure of the calcined catalyst precursor, which would just yield the desired MnO-covered metallic cobalt after reduction [17,59].

As stated above, for the Mn-promoted catalysts, the positive effect of pressure on activity and selectivity only holds up to a pressure of 4 bar after which a maximum is reached and a negative effect of increasing pressure on the product distribution is seen. It

is uncertain why a similar pressure dependence has not been reported before in literature. The group of Bell reports a continuous increase in reaction rate with total pressure, but observed a peculiar maximum in rate at about 1 bar CO partial pressure [18], which would be roughly in line with 4 bar total pressure at a H_2/CO ratio of 2. The occurrence of a maximum can be explained by taking into account that MnO catalyzes the CO dissociation and CH_x formation, but not C–C coupling. On the unpromoted Co catalyst, the CO dissociation sites are the same as the chain-growth sites, viz. step-edge sites [60–65] and enhanced CH_x formation at increasing pressure will immediately lead to an increased chain growth rate. However, on Mn-promoted catalysts, the CH_x monomers are formed at the interface of MnO and Co and have to migrate to chain-growth sites on the metallic cobalt. In general, migration of surface adsorbates is easy on empty Co surfaces [66,67]. Increasing the pressure, however, increases the coverage of adsorbed species other than CH_x and most prominently CO, which might hinder the migration of CH_x monomers. Apparently, this hindrance starts to dominate over the positive effect of Mn on the CO dissociation rate at pressures above 4 bar. Methane formation does not require stepped sites but occurs on sites that cover the majority of the surface [56] and does thus not rely on migration. As a consequence, the methane selectivity is rather independent of the pressure. This results in a maximum C_{5+} selectivity and thus also to a minimum in the selectivity to other products like of CH_4 and C_2-C_4 hydrocarbons at 4 bar. The hypothesis that the MnO-Co interface site does not catalyze chain growth also explains the observation that at high pressures, at which the metal sites but not the Mn promoted sites are poisoned by adsorbed CO, the C_{5+} selectivity is not enhanced by Mn addition.

5. Conclusions

In this study Mn-promoted Co catalysts on silica were studied in the FT reaction in a pressure range from 2 to 20 bar. After reduction of the oxidic catalyst precursor at 450 °C, metallic cobalt particles are formed, which are decorated with MnO. *In situ* IR spectroscopy and SSITKA measurements indicate that the presence of Mn enhances the CO dissociation and hydrocarbon formation. DFT calculations on an MnO/Co(0001) model cluster shows that CO can be activated by vacancies in the Mn oxide with a lower activation energy than on regular step-edge sites. At low pressure, Mn promotion results in a higher activity and C_{5+} selectivity, which both can be explained by the increased CO activation rate and resulting higher monomer coverage. At high pressure, however, Mn promotion results in a lower C_{5+} selectivity. This is a result of peculiar differences in pressure dependence between the unpromoted and Mn-promoted catalysts. Increasing pressure leads to an increased activity and C_{5+} selectivity for the unpromoted Co catalyst. The Mn promoted catalyst shows the same trend but only up to 4 bar. Above this pressure, the activity stabilizes and the C_{5+} selectivity drops dramatically at increasing pressure. This behavior is tentatively ascribed to hindered migration of CH_x growth monomers at increasing pressure. On unpromoted Co catalysts, the catalytic site for CO dissociation and chain growth is the same, viz, a stepped site. Mn promotion enhances CO dissociation but likely not C–C coupling. Hence, CH_x fragments formed at the Co-MnO interface have to migrate to stepped sites for chain growth. This migration can be hindered by surface adsorbates. Since the coverage of adsorbed reactants and intermediates increases with pressure, an higher reaction pressure can suppress migration and chain growth. Apparently, the hindrance of migration by adsorbed species dominates at pressures above 4 bar, leading to a decreasing C_{5+} selectivity. As a consequence, Mn promotion on silica-supported Co at low pressure leads to an increase in chain-growth probability, while it decreases the C_{5+} selectivity at high pressure.

Data availability

No data was used for the research described in the article.

Declaration of Competing Interest

The authors declare that they have no known competing financial interests or personal relationships that could have appeared to influence the work reported in this paper.

Acknowledgment

We acknowledge financial support by a NWO-TOP grant awarded to Emiel J. M. Hensen.

Appendix A. Supplementary material

Supplementary data to this article can be found online at https://doi.org/10.1016/j.jcat.2023.06.010.

References

[1] M.E. Dry, J.C. Hoogendoorn, Technology of the Fischer-Tropsch process, Catal. Rev. 23 (1–2) (1981) 265–278.
[2] M.E. Dry, The Fischer-Tropsch process: 1950–2000, Catal. Today 71 (3) (2002) 227–241.
[3] H. Schulz, Short history and present trends of Fischer-Tropsch synthesis, Appl. Catal. A Gen. 186 (1–2) (1999) 3–12.
[4] C.J. Weststrate, P. van Helden, J.W. Niemantsverdriet, Reflections on the Fischer-Tropsch synthesis: mechanistic issues from a surface science perspective, Catal. Today 275 (2016) 100–110.
[5] A.Y. Khodakov, W. Chu, P. Fongarland, Advances in the development of novel cobalt Fischer-Tropsch catalysts for synthesis of long-chain hydrocarbons and clean fuels, Chem. Rev. 107 (5) (2007) 1692–1744.
[6] G.R. Johnson, A.T. Bell, Effects of lewis acidity of metal oxide promoters on the activity and selectivity of Co-based Fischer-Tropsch synthesis catalysts, J. Catal. 338 (2016) 250–264.
[7] F. Morales, F.M.F. de Groot, P. Glatzel, E. Kleimenov, H. Bluhm, M. Hävecker, A. Knop-Gericke, B.M. Weckhuysen, In situ X-ray absorption of Co/Mn/TiO_2 catalysts for Fischer–Tropsch synthesis, J. Phys. Chem. B 108 (41) (2004) 16201–16207.
[8] F. Morales, F.M.F. de Groot, O.L.J. Gijzeman, A. Mens, O. Stephan, B.M. Weckhuysen, Mn promotion effects in Co/TiO_2 Fischer-Tropsch catalysts as investigated by XPS and STM-EELS, J. Catal. 230 (2) (2005) 301–308.
[9] F. Morales, D. Grandjean, F.M.F. de Groot, O. Stephan, B.M. Weckhuysen, Combined EXAFS and STEM-EELS study of the electronic state and location of Mn as promoter in Co-based Fischer-Tropsch catalysts, Phys. Chem. Chem. Phys. 2005 (7) (2005) 568–572.
[10] F. Morales, D. Grandjean, A. Mens, F.M.F. de Groot, B.M. Weckhuysen, X-ray absorption spectroscopy of Mn/Co/TiO_2 Fischer-Tropsch catalysts: relationships between preparation method, molecular structure, and catalyst performance, J. Phys. Chem. B 110 (2006) 8626–8639.
[11] G.L. Bezemer, P.B. Radstake, U. Falke, H. Oosterbeek, H.P.C.E. Kuipers, A.J. van Dillen, K.P. de Jong, Investigation of promoter effects of manganese oxide on carbon nanofiber-supported cobalt catalysts for Fischer-Tropsch synthesis, J. Catal. 237 (1) (2006) 152–161.
[12] F. Morales, E. de Smit, F.M.F. de Groot, T. Visser, B.M. Weckhuysen, Effects of manganese oxide promoter on the CO and H_2 adsorption properties of titania-supported cobalt Fischer-Tropsch catalysts, J. Catal. 2007 (246) (2007) 91–99.
[13] G.L. Bezemer, J.H. Bitter, H.P.C.E. Kuipers, H. Oosterbeek, J.E. Holewijn, X. Xu, F. Kapteijn, A.J. van Dillen, K.P. de Jong, Cobalt particle size effects in the Fischer-Tropsch reaction studied with carbon nanofiber supported catalysts, J. Am. Chem. Soc. 128 (12) (2006) 3956–3964, https://doi.org/10.1021/ja058282w.
[14] J. Barrault, A. Guilleminot, J.C. Achard, V. Paul-Boncour, A. Percheron-Guegan, Hydrogenation of carbon monoxide on carbon-supported cobalt rare earth catalysts, Appl. Catal. 21 (2) (1986) 307–312.
[15] J. Barrault, A. Guilleminot, J.C. Achard, V. Paul-Boncour, A. Percheron-Guegan, L. Hilaire, M. Coulon, Syngas reaction over lanthanum-cobalt intermetallic catalysts, Appl. Catal. 22 (2) (1986) 273–287.
[16] A. Boffa, C. Lin, A.T. Bell, G.A. Somorjai, Promotion of CO and CO_2 hydrogenation over Rh by metal oxides: the influence of oxide Lewis acidity and reducibility, J. Catal. 149 (1) (1994) 149–158.
[17] A. Dinse, M. Aigner, M. Ulbrich, G.R. Johnson, A.T. Bell, Effects of Mn promotion on the activity and selectivity of Co/SiO_2 for Fischer-Tropsch synthesis, J. Catal. 288 (2012) 104–114.

[18] G.R. Johnson, S. Werner, A.T. Bell, An investigation into the Effects of Mn promotion on the activity and selectivity of Co/SiO_2 for Fischer-Tropsch synthesis: evidence for enhanced CO adsorption and dissociation, ACS Catal. 5 (10) (2015, 2015,) 5888–5903.
[19] L. Zhong, F. Yu, Y. An, Y. Zhao, Y. Sun, Z. Li, T. Lin, Y. Lin, X. Qi, Y. Dai, L. Gu, J. Hu, S. Jin, Q. Shen, H. Wang, Cobalt carbide nanoprisms for direct production of lower olefins from syngas, Nature 538 (7623) (2016) 84–87.
[20] M. Athariboroujeny, A. Raub, V. Iablokov, S. Chenakin, L. Kovarik, N. Kruse, Competing mechanisms in CO hydrogenation over $Co\text{-}MnO_x$ catalysts, ACS Catal. 9 (6) (2019, 2019,) 5603–5612.
[21] I.A.W. Filot, R.A. van Santen, E.J.M. Hensen, The optimally performing Fischer-Tropsch catalyst, Angew. Chemie Int. Ed. 53 (47) (2014) 12746–12750.
[22] D. Schanke, S. Vada, E.A. Blekkan, A.M. Hilmen, A. Hoff, A. Holmen, Study of Pt-promoted cobalt CO hydrogenation catalysts, J. Catal. 156 (1) (1995) 85–95.
[23] W. Chen, I.A.W. Filot, R. Pestman, E.J.M. Hensen, Mechanism of cobalt-catalyzed CO hydrogenation: 2, Fischer-Tropsch synthesis, ACS Catal. 7 (12) (2017) 8061–8071.
[24] P. Biloen, J.N. Helle, W.M.H. Sachtler, Incorporation of surface carbon into hydrocarbons during Fischer-Tropsch synthesis: mechanistic implications, J. Catal. 58 (1) (1979) 95–107.
[25] P.E. Blöchl, O. Jepsen, O.K. Andersen, Improved tetrahedron method for Brillouin-zone integrations, Phys. Rev. B 49 (23) (1994) 16223–16233.
[26] J.P. Perdew, K. Burke, M. Ernzerhof, Generalized gradient approximation made simple, Phys. Rev. Lett. 77 (18) (1996) 3865–3868.
[27] G. Kresse, J. Hafner, Ab initio molecular dynamics for liquid metals, Phys. Rev. B 47 (1) (1993) 558–561.
[28] G. Kresse, J. Furthmüller, Efficient iterative schemes for ab initio total-energy calculations using a plane-wave basis set, Phys. Rev. B - Condens. Matter Mater. Phys. 54 (16) (1996) 11169–11186.
[29] W.L. Vrijburg, E. Moioli, W. Chen, M. Zhang, B.J.P. Terlingen, B. Zijlstra, I.A.W. Filot, A. Züttel, E.A. Pidko, E.J.M. Hensen, Efficient base-metal $NiMn/TiO_2$ catalyst for CO_2 methanation, ACS Catal. 9 (9) (2019) 7823–7839.
[30] J.D. Pack, H.J. Monkhorst, "Special points for Brillouin-zone integrations" -a reply, Phys. Rev. B 16 (4) (1977) 1748–1749.
[31] K. Sun, Y. Zhao, H.Y. Su, W.X. Li, Force reversed method for locating transition states, Theor. Chem. Acc. 131 (2) (2012) 1–10.
[32] G. Henkelman, B.P. Uberuaga, H. Jónsson, Climbing image nudged elastic band method for finding saddle points and minimum energy paths, J. Chem. Phys. 113 (22) (2000) 9901–9904.
[33] G. Henkelman, H. Jónsson, Improved tangent estimate in the nudged elastic band method for finding minimum energy paths and saddle points, J. Chem. Phys. 113 (22) (2000) 9978–9985, https://doi.org/10.1063/1.1323224.
[34] J. P. den Breejen, A. M. Frey, J. Yang, A. Holmen, M. M. van Schooneveld, F. M. F. de Groot.
[35] J.X. Liu, J.H.Y. Su, D.P. Sun, B.Y. Zhang, W.X. Li, Crystallographic dependence of CO activation on cobalt catalysts: HCP versus FCC, J. Am. Chem. Soc. 135 (44) (2013) 16284–16287.
[36] S.E. Colley, R.G. Copperthwaite, G.J. Hutchings, Unusual cobalt phases in CO-hydrogenation catalysts, studies by in-situ X-ray diffraction, Catal. Today 9 (1–2) (1991) 203–209.
[37] O.A. Bulavchenko, E.Y. Gerasimov, T.N. Afonasenko, Reduction of double manganese-cobalt oxides: in situ XRD and TPR study, Dalt. Trans. 47 (47) (2018) 17153–17159.
[38] M.C. Biesinger, B.P. Payne, A.P. Grosvenor, L.W.M. Lau, A.R. Gerson, R.S.C. Smart, Resolving surface chemical states in XPS analysis of first row transition metals, oxides and hydroxides: Cr, Mn, Fe, Co and Ni, Appl. Surf. Sci. 257 (7) (2011) 2717–2730.
[39] V.R. Galakhov, M. Demeter, S. Bartkowski, M. Neumann, N.A. Ovechkina, E.Z. Kurmaev, N.I. Lobachevskaya, Y.M. Mukovskii, J. Mitchell, D.L. Ederer, Mn 3s exchange splitting in mixed-valence manganites, Phys. Rev. B 65 (11) (2002).
[40] M. Chigane, M. Ishikawa, Manganese oxide thin film preparation by potentiostatic electrolyses and electrochromism, J. Electrochem. Soc. 147 (6) (2000) 2246.
[41] A.J. Nelson, J.G. Reynolds, J.W. Roos, Core-level satellites and outer core-level multiplet splitting in Mn model compounds, J. Vac. Sci. Technol. A 18 (4) (2000) 1072–1076.
[42] M. Huynh, C. Shi, S.J.L. Billinge, D.G. Nocera, Nature of activated manganese oxide for oxygen evolution, J. Am. Chem. Soc. 137 (47) (2015) 14887–14904.
[43] R.G. Copperthwaite, G.J. Hutchings, M. van der Riet, J. Woodhouse, Carbon monoxide hydrogenation using manganese oxide based catalysts: effect of operating conditions on alkene selectivity, Ind. Eng. Chem. Res. 26 (5) (1987) 869–874.
[44] S. Colley, R.G. Copperthwaite, G.J. Hutchings, M. van der Riet, Carbon monoxide hydrogenation using cobalt manganese oxide catalysts: initial catalyst optimization studies, Ind. Eng. Chem. Res. 27 (8) (1988) 1339–1344.
[45] M. van der Riet, G.J. Hutchings, R.G. Copperthwaite, Selective formation of C_3 hydrocarbons from $CO + H_2$ using cobalt–manganese oxide catalysts, J. Chem. Soc. Chem. Commun. (10) (1986) 798–799.
[46] S. L. Soled, W. Iglesia, R.A. Fiato, Copper-promoted cobalt-manganese spinel catalyst for Fischer-Tropsch synthesis of lower alkenes, US Patent 5162284 (1992).
[47] G.R. Johnson, S. Werner, K.C. Bustillo, P. Ercius, C. Kisielowski, A.T. Bell, Investigations of element spatial correlation in Mn-promoted Co-based Fischer-Tropsch synthesis catalysts, J. Catal. 328 (2015) 111–122.
[48] G. Bezemer, P. Radstake, U. Falke, H. Oosterbeek, H. Kuipers, A. Vandillen, K. Dejong, Investigation of promoter effects of manganese oxide on carbon nanofiber-supported cobalt catalysts for Fischer-Tropsch synthesis, J. Catal. 237 (1) (2006) 152–161.
[49] W. Chen, R. Pestman, B. Zijlstra, I.A.W. Filot, E.J.M. Hensen, Mechanism of cobalt-catalyzed CO hydrogenation: 1, Methanation, ACS Catal. 7 (12) (2017) 8050–8060.
[50] M. Zhuo, A. Borgna, M. Saeys, Effect of the CO coverage on the Fischer-Tropsch synthesis mechanism on cobalt catalysts, J. Catal. 297 (2013) 217–226.
[51] W. Chen, B. Zijlstra, I.A.W. Filot, R. Pestman, E.J.M. Hensen, Mechanism of carbon monoxide dissociation on a cobalt Fischer-Tropsch catalyst, ChemCatChem 10 (1) (2018) 136–140.
[52] G.A. Beitel, A. Laskov, H. Oosterbeek, E.W. Kuipers, Polarization modulation infrared reflection absorption spectroscopy of CO adsorption on Co(0001) under a high-pressure regime, J. Phys. Chem. 100 (30) (1996) 12494–12502.
[53] C.J. Weststrate, J. van de Loosdrecht, J.W. Niemantsverdriet, Spectroscopic insights into cobalt-catalyzed Fischer-Tropsch synthesis: a review of the carbon monoxide interaction with single crystalline surfaces of cobalt, J. Catal. 342 (2016) 1–16.
[54] R.L. Toomes, D.A. King, The Adsorption of CO on Co(1010), Surf. Sci. 349 (1) (1996) 1–18.
[55] Y. Zhu, X. Pan, F. Jiao, J. Li, J. Yang, M. Ding, Y. Han, Z. Liu, X. Bao, Role of manganese oxide in syngas conversion to light olefins, ACS Catal. 7 (4) (2017) 2800–2804.
[56] R. Pestman, W. Chen, E.J.M. Hensen, Insight into the rate-determining step and active sites in the Fischer-Tropsch reaction over cobalt catalysts, ACS Catal. 9 (5) (2019) 4189–4195.
[57] A.J. Markvoort, R.A. van Santen, P.A.J. Hilbers, E.J.M. Hensen, Kinetics of the Fischer-Tropsch reaction, Angew. Chemie - Int. Ed. 51 (36) (2012) 9015–9019.
[58] I.D. Brown, A. Skowron, Electronegativity and Lewis acid strength, J. Am. Chem. Soc. 112 (9) (1990) 3401–3403.
[59] M. Athariboroujeny, A. Raub, V. Iablokov, S. Chenakin, L. Kovarik, N. Kruse, Competing mechanisms in co hydrogenation over $co\text{-}MnO_x$ catalysts, ACS Catal. 9 (2019) 5603–5612.
[60] J.J.C. Geerlings, M.C. Zonnevylle, C.P.M. de Groot, Structure sensitivity of the Fischer-Tropsch reaction on cobalt single crystals, Surf. Sci. 241 (3) (1991) 315–324.
[61] C. Qin, B. Hou, J. Wang, Q. Wang, G. Wang, M. Yu, C. Chen, L. Jia, D. Li, Crystal-plane-dependent Fischer-Tropsch performance of cobalt catalysts, ACS Catal. 8 (10) (2018) 9447–9455.
[62] Z.P. Liu, P. Hu, A new insight into Fischer-Tropsch synthesis, J. Am. Chem. Soc. 124 (39) (2002) 11568–11569.
[63] S.G. Shetty, I.M. Ciobîcă, E.J.M. Hensen, R.A. van Santen, Site regeneration in the Fischer-Tropsch synthesis reaction: a synchronized co dissociation and C-C coupling pathway, Chem. Commun. (Camb) 47 (35) (2011) 9822–9824.
[64] B. Zijlstra, R.J.P. Broos, W. Chen, H. Oosterbeek, I.A.W. Filot, E.J.M. Hensen, Coverage effects in CO dissociation on metallic cobalt nanoparticles, ACS Catal. 9 (8) (2019) 7365–7372.
[65] B. Zijlstra, R.J.P. Broos, W. Chen, G.L. Bezemer, I.A.W. Filot, E.J.M. Hensen, The vital role of step-edge sites for both CO activation and chain growth on cobalt Fischer-Tropsch catalysts revealed through first-principles-based microkinetic modeling including lateral interactions, ACS Catal. 10 (16) (2020) 9376–9400.
[66] J.C.W. Swart, I.M. Ciobîcă, R.A. van Santen, E. van Steen, Intermediates in the formation of graphitic carbon on a flat FCC-Co(111) surface, J. Phys. Chem. C 112 (33) (2008) 12899–12904.
[67] L. Joos, I.A.W. Filot, S. Cottenier, E.J.M. Hensen, M. Waroquier, V. van Speybroeck, R.A. van Santen, Reactivity of CO on carbon-covered cobalt surfaces in Fischer-Tropsch synthesis, J. Phys. Chem. C 118 (10) (2014) 5317–5321.